

Geochemistry, Geophysics, Geosystems®

RESEARCH ARTICLE

10.1029/2023GC011167

Key Points:

- The provenance of a Paleogene (35–27 Ma) eolian dust sequence in Ulanatal, Inner Mongolia, China, reveals a modern-type eolian regime
- Global cooling and possibly expansion of Northern Hemisphere ice volume modulated the dust provenance by strengthening the Siberian High
- Long-term negative (positive) phase of Arctic Oscillation-like conditions were favored in the warmhouse Eocene (coolhouse Oligocene)

Supporting Information:

Supporting Information may be found in the online version of this article.

Correspondence to:

K. Bohm,
katja.bohm@helsinki.fi

Citation:

Bohm, K., Wasiljeff, J., Stevens, T., Salminen, J., Tang, H., Lahaye, Y., et al. (2024). Modern-type eolian regime and global cooling-modulated dust provenance in the late Paleogene of Central-East Asia. *Geochemistry, Geophysics, Geosystems*, 25, e2023GC011167. <https://doi.org/10.1029/2023GC011167>

Received 1 AUG 2023

Accepted 23 JAN 2024

Author Contributions:

Conceptualization: K. Bohm, T. Stevens, H. Tang, A. Kaakinen

Data curation: K. Bohm

Formal analysis: K. Bohm

Funding acquisition: T. Stevens, A. Kaakinen

Investigation: K. Bohm, J. Wasiljeff, Y. Lahaye, M. Kurhila, O. Haugvaldstad

Methodology: K. Bohm, J. Wasiljeff, T. Stevens, J. Salminen, H. Tang, Y. Lahaye, M. Kurhila, A. Kaakinen

Project administration: T. Stevens, A. Kaakinen

© 2024 The Authors. *Geochemistry, Geophysics, Geosystems* published by Wiley Periodicals LLC on behalf of American Geophysical Union.

This is an open access article under the terms of the [Creative Commons Attribution License](#), which permits use, distribution and reproduction in any medium, provided the original work is properly cited.

Modern-Type Eolian Regime and Global Cooling-Modulated Dust Provenance in the Late Paleogene of Central-East Asia

K. Bohm^{1,2} , J. Wasiljeff^{1,3} , T. Stevens^{1,2} , J. Salminen^{1,3} , H. Tang^{1,4,5} , Y. Lahaye³ , M. Kurhila³ , Z. Zhang^{6,7,8} , O. Haugvaldstad^{5,9} , and A. Kaakinen¹ 

¹Department of Geosciences and Geography, University of Helsinki, Helsinki, Finland, ²Department of Earth Sciences, Uppsala University, Uppsala, Sweden, ³Geological Survey of Finland, Espoo, Finland, ⁴Finnish Meteorological Institute, Climate System Research, Helsinki, Finland, ⁵Department of Geosciences, University of Oslo, Oslo, Norway, ⁶Key Laboratory of Vertebrate Evolution and Human Origin of the Chinese Academy of Sciences, Institute of Vertebrate Paleontology and Paleoanthropology, Chinese Academy of Sciences, Beijing, China, ⁷CAS Center for Excellence in Life and Paleoenvironment, Beijing, China, ⁸University of Chinese Academy of Sciences, Beijing, China, ⁹Norwegian Meteorological Institute, Oslo, Norway

Abstract Atmospheric mineral dust is a poorly constrained yet extremely important component of the climate system. Provenance studies from geologic dust archives are crucial to understand the drivers of the dust cycle over long time scales. Our multi-technique provenance analysis of a rare Paleogene (35–27 Ma) eolian dust sequence from Ulanatal, ~400 km northwest of the Chinese Loess Plateau (CLP), shows that Paleogene dust transporting winds generally varied between northwesterly and westerly, the same as those in the late Neogene-Quaternary bipolar icehouse. We propose that, as today, westerly wind circulation patterns would have been modulated by an Arctic Oscillation (AO)-like situation, and that the warm Eocene favored a long-term negative phase of AO, leading to meridional westerly circulation and the dominance of a northwesterly dust transport pathway. After the Eocene-Oligocene transition (EOT), long-term positive phase of AO-like conditions initiated, leading to stronger and more zonal westerlies. The Siberian High (SH) also formed or strengthened at the EOT and started to control dust storm activity along the northwesterly transport pathway. We argue that increased Paleogene Northern Hemisphere (NH) ice volume was the ultimate driver of this modern-type dust transport regime in the Ulanatal region, possibly also controlling initial Ulanatal dust sequence formation via the development of the SH and modern-type eolian regime. The similarity between the Ulanatal and late Neogene northern CLP dust provenance signals suggests that the increased NH ice volume, via its control on the northwesterly dust transport, could have promoted increased loess formation also in the late Miocene.

Plain Language Summary Understanding the effects and responses of atmospheric mineral dust to climate changes in the geologic past is crucial for predicting future scenarios. Analysis of the source of dust deposited 35–27 million years ago in Ulanatal, Inner Mongolia, China reveals that the Central-East Asian atmospheric circulation during this time interval was similar to that of today. Specifically, dust transport was dominated by northwesterly and westerly winds despite a significantly warmer global climate. We also propose that Arctic Oscillation (AO)-type conditions, stemming from the temperature difference between the high and low latitudes, modulated planetary westerly winds during this period. Our results suggest that during warmer phases, a negative AO type dominated and resulted in wave-like westerly wind patterns and a northwesterly dust transport pathway to Ulanatal. During cooler phases, the westerly circulation became stronger and more zonal. The Siberian High pressure system was possibly strengthened during increased Northern Hemisphere (NH) ice volume and further affected northwesterly dust transport. Our findings suggest that NH ice volume increase was possibly also responsible for the formation of the Ulanatal dust sequence itself. Our results imply that even under significantly warmer conditions than today, polar ice affects the long-term dustiness in this highly populated region.

1. Introduction

Understanding the atmospheric circulation during various global climate states in the geologic past is crucial for investigating the drivers and consequences of long-term climate evolution. As an important component in the Earth system, wind-blown mineral dust (hereby “dust”) links the atmosphere to the geosphere, and both affects

Resources: J. Wasiljeff, J. Salminen, Z. Zhang, A. Kaakinen
Supervision: T. Stevens, A. Kaakinen
Visualization: K. Bohm, O. Haugvaldstad
Writing – original draft: K. Bohm
Writing – review & editing: K. Bohm, J. Wasiljeff, T. Stevens, J. Salminen, H. Tang, Y. Lahaye, M. Kurhila, Z. Zhang, O. Haugvaldstad, A. Kaakinen

and is affected by changes in climate (e.g., Adebisi & Kok, 2020; Lu et al., 2010; Martin, 1990; Tegen et al., 1996). Central-East Asian eolian dust deposits provide exceptional opportunities to study the interactions between climate, tectonics and dust since the early Eocene (J. X. Li et al., 2018). The deposition and in situ alteration of the well-studied Quaternary and late Neogene deposits of the Chinese Loess Plateau (CLP) have been linked to the East Asian monsoon (EAM) and planetary westerly circulation (e.g., An, 2000; Lu et al., 2019; Wen et al., 2005). However, the scarcity of older dust deposits has hampered our understanding of the pre-late Neogene Asian dust cycle and associated atmospheric circulation in periods of significantly warmer climates than today.

Central-East Asian dust transport today mainly occurs via two pathways: (a) westerly winds passing through major dust source regions, such as the Taklamakan desert and Northern Tibetan Plateau (NTP); (b) northwesterly winds blowing through the dry regions in Mongolia and northwestern-northern China (Figure 1a; e.g. Chen et al., 2017). While the westerly pathway is driven by planetary westerlies, the modern northwesterly pathway is primarily driven by the East Asian trough and the increased winter land-sea thermal contrast that produces the anticyclonic Siberian High (SH) pressure system, and its associated East Asian winter monsoon (EAWM; defined as pressure difference between the SH and Aleutian Low, or low-level northwesterly wind over East Asia). However, northwesterly winds over midlatitude Asia today may also be associated with a more meandering prevailing westerly wind circulation (Figure 1a) during negative phases of the Arctic Oscillation (AO; He et al., 2017). Negative AO is favored during warm conditions in the Arctic region. Transient, surface-level cyclonic eddies (low pressure systems) over Mongolia are a pre-requisite for dust storm events along this northwesterly pathway, as they enable dust emission and advection to the higher troposphere, enabling longer distance transport (Shao & Wang, 2003). Large, mostly spring-time (Kurosaki & Mikami, 2003) dust storms are produced when cold outbreaks following these cyclones and guided by the East Asian trough, produce strong northwesterly winds (Shao & Wang, 2003). On the synoptic (season average) scale, such circulation is often associated with a negative AO phase (e.g., Mao et al., 2011) and sometimes, a strong EAWM (Wyrwoll et al., 2016; Y. Zhang et al., 1997). In summary, the phase of AO, which ultimately stems from the temperature gradient between the high and low latitudes, and the strength of SH/EAWM, both directly affect the two dominant modern dust transport pathways (planetary/prevaling westerlies and northwesterly winds) in Central-East Asia.

On longer time scales, the Neogene Red Clay and the Quaternary loess deposits across the CLP are believed to have dominantly formed from northwesterly wind-transported dust as a response to global cooling and the expansion of the Northern Hemisphere (NH) ice sheets, especially at the onset of the Quaternary (e.g., Bohm et al., 2023a; Wen et al., 2005; H. Zhang et al., 2022). Westerly winds (upper or lower level), however, seem to have dominated the dust transport to the western parts of the CLP (Shang et al., 2016) and the North Pacific Ocean (Nie et al., 2018; Rea et al., 1998), the latter exhibiting Quaternary dust fluxes that are highest during glacial periods (Abell et al., 2023). It is not uncommon in the literature (e.g., Bohm et al., 2023a) to allocate this Neogene-Quaternary northwesterly dust transport to the EAWM, even though the major dust events occur in the spring (Roe, 2009) and as stated above, the reality of northwesterly wind dust transport is likely more complicated. However, the EAWM, the SH, cold surges following low pressure systems, the AO, and the westerlies are all linked, despite their teleconnections being not well constrained (e.g., He et al., 2017).

Considerable debate exists over the onset and evolution of EAM circulation (e.g., X. Li et al., 2018a; Spicer et al., 2017; Tardif et al., 2020; R. Zhang et al., 2018), with some evidence pointing to the existence of an EAM (or EAM-type wind pattern) in the Eocene (Licht et al., 2014), or even already in the Cretaceous (Farnsworth et al., 2019). Dust provenance analysis is one of the few ways to reconstruct past dust transport trajectories and to reveal the prevailing wind directions and the possible existence of any Paleogene EAWM. Indeed, the existence of Eocene midlatitude planetary westerlies as dust conveyors to the Xining Basin on the western CLP margin and to the Xorkol Basin in western China have been inferred from dust provenance studies (Licht, Dupont-Nivet, et al., 2016; Pan et al., 2023). However, it is difficult to reconstruct regional scale circulation patterns from individual sites, and further analyses on deposits located closer to the core SH region are needed to fully test the existence of EAWM-linked northerly/northwesterly dust transport. Furthermore, the role of the Paratethys Sea in controlling moisture balance and atmospheric circulation during the Paleogene remains unclear. While westerly winds likely transported Paratethys Sea moisture to NE Tibet and Central Asia (Caves et al., 2015; Meijer et al., 2019), general increased aridity in the region may have already been established in the Eocene, as suggested by paleoprecipitation and -environmental proxies, and the existence of Paleogene dust deposits (Abels et al., 2011; Bosboom et al., 2014; J. X. Li et al., 2018; X. Li et al., 2018b; Licht, Dupont-Nivet, et al., 2016; Wasiljeff et al., 2020).

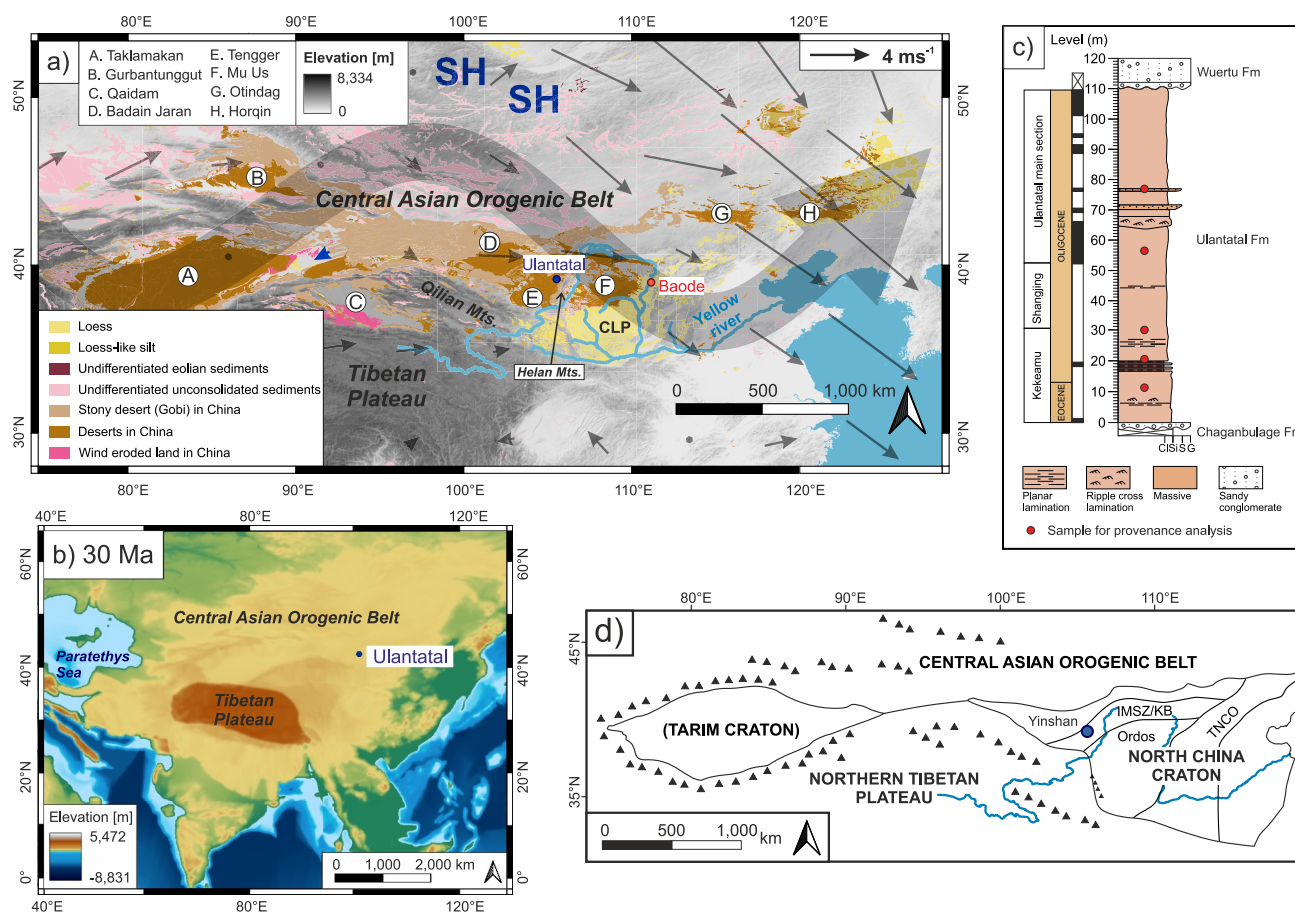


Figure 1. (a) Digital elevation model (Shuttle Radar Topography Mission), and the modern locations of Paleogene Ulanatal sequence, Neogene-Quaternary Baode Red Clay-loess, deserts, and dry areas in the study region. The distribution of loess, loess-like silt, and the undifferentiated sediments are from Börker et al. (2018), and the deserts and wind eroded land in China from 1:200,000 Desert Distribution Data set provided by the Environmental and Ecological Science Data Center for West China, the National Natural Science Foundation of China (<http://westdcwestgis.ac.cn>, last access 27 July 2020). Siberian High (SH) denotes the approximate location of the SH pressure system. The single large arrow is figurative and illustrates the westerly circulation pattern during a negative phase of Arctic Oscillation. Smaller arrows denote winter (December-February) surface wind direction and relative strength plotted from ERA5 data (20 years average; Hersbach et al., 2023). One northeasterly wind component at latitude $\sim 40^\circ\text{N}$ is highlighted with a dark blue color. CLP = Chinese Loess Plateau. (b) Paleogeographic digital elevation model map showing the location of Ulanatal, Tibetan Plateau, and the Paratethys Sea at 30 Ma. The map was produced with the QGIS plugin Terra Antiqua (Aminov et al., 2023) and the paleolatitude (42.4°N) of Ulanatal site was exported from the associated Paleoenvironment map website (<https://map.paleoenviroment.eu/>—last access 5 October 2023). (c) A simplified composite lithological column (after Wasiljeff et al., 2022) of the Ulanatal site with subsections, sediment thickness of the Ulanatal Formation, epochs and polarity zones correlated with Gradstein et al. (2005). DZ-DR sampling locations are indicated with red circles. (d) Schematic map of the simplified tectonic divisions of the study area after Bohm et al. (2023a) and the location of Ulanatal (blue circle). IMSZ/KB = Inner Mongolia Suture Zone/Khondalite Belt. TNCO = Trans-North China Orogen.

In this paper, we study the provenance of a rare Eocene-Oligocene (c. 35–27 Ma; Wasiljeff et al., 2020) eolian dust sequence located in Ulanatal, Inner Mongolia, China. Due to its location near the core SH region, the Ulanatal site likely recorded both the westerly and any SH-induced northerly/northwesterly dust transport to CLP. Furthermore, Ulanatal is (and was) located relatively far away from the Tibetan Plateau (TP; Figures 1a and 1b), reducing the likelihood of its dust provenance being controlled by TP tectonic evolution. The Ulanatal dust sequence covers the Eocene-Oligocene Transition (EOT; c. 34 Ma), which marks the dramatic global shift from warmhouse to coolhouse state as permanent ice sheets appeared on Antarctica (e.g., Coxall et al., 2005; Westerhold et al., 2020) and may have stabilized in eastern Greenland (Tripathi & Darby, 2018). While there are sites (Xining, Lanzhou, and Weihe Basins) in Central-East Asia that record the EOT as an episode of significant drying (Abels et al., 2011; Ao et al., 2020; Dupont-Nivet et al., 2007; Y. Wang et al., 2023), the climate in Ulanatal remained remarkably stable through the transition (Wasiljeff et al., 2022). Rather, major aridification events in Ulanatal are recorded in precipitation proxies after the EOT, at c. 31 and 28 Ma, roughly corresponding to the Early Oligocene Aridification Event (EOAE) and the Mid-Oligocene Reorganization of fauna in Central Asia (Harzhauser et al., 2016), respectively (Wasiljeff et al., 2022). Constraining the provenance of the Ulanatal dust

sequence is crucial for testing wider patterns of Paleogene aridification in Central Asia, as sediment provenance may strongly affect paleoclimatic proxies through for example, mineralogy and grain size.

This paper combines anisotropy of magnetic susceptibility (AMS), single-grain detrital zircon (DZ) U-Pb dating, and single-grain detrital rutile (DR) trace element geochemistry with dust source contribution models. Recent studies have highlighted the need for such a multi-technique provenance analysis (e.g., Bohm et al., 2022; Fenn et al., 2018; Y. Sun et al., 2020). While DZ ages have been widely used in previous CLP provenance studies (e.g., Bird et al., 2015; Nie et al., 2015, 2018; Shang et al., 2016; Stevens et al., 2010, 2013; H. Zhang et al., 2022), DRs have recently been shown to be a powerful complement to DZs in provenance studies on the late Neogene CLP dust (Bohm et al., 2022, 2023a). In this study, we apply the AMS to indicate the surface wind directions, and the detrital mineral analyses to explore the mixed Ulanatal dust provenance. As such, this study aims to test the controls on late Paleogene Asian dust deposition and transport, and infer the evolution of the associated wind regime on long time scales and under warmer climates.

2. Geologic Setting

The Ulanatal site is located in Bayanhot Basin, approximately 400 km NW of the central CLP, and 50 km west of the N-NE trending Helan Mts (Figure 1a). The crystalline basement rocks in this region belong to the Proterozoic Inner Mongolia Suture Zone/Khondalite Belt, which divides the western part of the North China Craton (NCC) into Ordos and Yinshan (Alxa) Blocks (Figure 1d). Based on apatite fission track dating, the adjacent Helan Mts. were rapidly uplifted in the Eocene (50–37 Ma; Zhao et al., 2007) and late Miocene (12–10 Ma; Liu et al., 2010). A minor uplift phase in the early Oligocene may also have occurred at ~30 Ma (Zhao et al., 2007).

The lithostratigraphy (Figure 1c), paleontology and environmental proxies of the Ulanatal dust sequences are described in detail by Wasiļjeff et al. (2020, 2022), Wasiļjeff and Zhang (2022), and Z. Zhang et al. (2016), and summarized in Text S1 in Supporting Information S1. The bulk of the Ulanatal Formation (Figure 1c) is interpreted to have an eolian origin based on its massive structure, grain size distributions, and laterally continuous lithologies (Wasiļjeff et al., 2020). The Ulanatal Formation unconformably overlies the Eocene Chaganbulage Formation and contains rich micromammalian faunas (Z. Zhang et al., 2016). The lowermost parts of the Ulanatal Formation consist of coarse silts and fine sands, with occasional thin parallel and ripple-cross laminations. The basal parts were interpreted as dominantly fluvial, and eolian deposition started by c. 34.8 Ma (Wasiļjeff et al., 2020). The overlying sedimentary succession is predominantly fine-grained, massive reddish yellow to reddish silt and clayey silt. Throughout the Ulanatal Formation, occasional calcareous beds are present, and an overall fining trend of median grain size is observed. The Miocene sandstones of the Wuertu Formation unconformably overlay the Ulanatal Formation, with a substantial erosional hiatus between (Z. Zhang et al., 2016).

3. Materials and Methods

3.1. Sample Collection and Preparation

The samples (5–8 kg) for the single-grain analyses were collected from five levels corresponding to eolian deposition at 34.2 (ZR2), 33.1 (ZR1), 32.5 (ZR3), 30.9 (ZR6), and ~29.3 (ZR7) Ma. The ages of the samples were constrained after Wasiļjeff et al. (2020). ZR7 was a composite sample (11 combined samples between 29.5 and 28.8 Ma, mean 29.3 Ma; ~1 kg total). The sample preparation techniques for DZ and DR analyses are outlined in Bohm et al. (2022).

Sampling for AMS is described in Wasiļjeff et al. (2020). Field observations indicate that the dust was deposited on a quasi-horizontal surface (Figure S1 in Supporting Information S1). AMS was measured from 362 samples with depositional ages between 34.8 and 26.8 Ma.

3.2. Anisotropy of Magnetic Susceptibility

The AMS was measured using a MFK1-FA Kappabridge (AGICO Inc., Brno, Czech Republic) at the Ivar Giaever Geomagnetic Laboratory, University of Oslo and at the Geological Survey of Finland (GTK) using a 200 A/m field at a 976 Hz frequency. The resulting AMS ellipsoids are defined by the orientation and magnitude of the principal susceptibility axes, $K_{\max} \geq K_{\text{int}} \geq K_{\min}$. Mass normalized magnetic susceptibility was taken from Wasiļjeff et al. (2022). Magnetic lineation (L) is defined by the alignment of K_{\max} and calculated as (Jelinek, 1981):

$$L = \frac{K_{\max}}{K_{\text{int}}}$$

Magnetic foliation (F) is expressed as

$$F = \frac{K_{\text{int}}}{K_{\min}}$$

The corrected degree of anisotropy (P_j) of AMS is defined as

$$P_j = \exp \sqrt{2 \left[(\eta_{\max} - \eta_{\text{mean}})^2 + (\eta_{\text{int}} - \eta_{\text{mean}})^2 + (\eta_{\min} - \eta_{\text{mean}})^2 \right]}$$

where the η parameter indicates the corresponding natural logarithms of the principal susceptibility values. The shape of the AMS ellipsoid is defined by T :

$$T = \frac{2\eta_{\text{int}} - \eta_{\max} - \eta_{\min}}{\eta_{\max} - \eta_{\min}}$$

An oblate AMS ellipsoid is defined by $1 > T > 0$, and a prolate ellipsoid by $-1 < T < 0$. If $T = 0$, the shape is neutral triaxial ellipsoid. The Jelinek diagram visualizes the relationship between T and P_j .

In order to apply AMS to infer paleowind interpretation in eolian dust/loess, it is important to identify the primary depositional magnetic fabric (MF) and consider the possible effects of reworking. The MF of loess may be influenced by multiple postdepositional processes, especially in areas where pedogenesis, reworking, slope creeping, freezing/thawing, or redeposition is likely (Lagroix & Banerjee, 2002). As such, we filter our data in order to (a) identify the primary depositional fabric and (b) pinpoint statistically significant anisotropy in individual datapoints, which may be indicative of dust transporting wind directions. We utilize the following specimen acceptance criteria (Hus, 2003; K  ltringer et al., 2021; Lagroix & Banerjee, 2004; Zhu et al., 2004) to achieve this: (a) Statistically significant F , defined by $F_{23} > 10$, vertical K_{\min} (inclination $> 70^\circ$), and sub-horizontal K_{\max} is present; (b) Statistically significant L , defined by $F_{12} > 4$ and $E_{12} < 20^\circ$ is present; (c) F is clearly higher than L and has similar trend to P_j when plotted against depth ($\rightarrow F$ controls the shape of the AMS ellipsoid); (d) The shape of the AMS ellipsoid is oblate ($T > 0$). (e) Stereoplot analysis and the principal susceptibility axes indicate gravity controlled and flow-aligned MF on a horizontal depositional plane. While these criteria may also be fulfilled by for example, undisturbed fluvial depositional environments, our data are collected from eolian units. The stereoplots were created using the software Anisoft 5.1.08 (AGICO Inc., Brno, Czech Republic), and their interpretation follows the MF types described by Brad  k et al. (2020).

Wasiljeff et al. (2020, 2022) provided detailed information on the magnetic properties of the Ulantatal sequence and showed that the dominant magnetic mineral in Ulantatal is single-domain and vortex state (prev. pseudo-single domain) magnetite with an additional contribution from hematite. Pedogenic magnetite/maghemite and hematite are also present. Based on changes in bulk magnetic properties (e.g., low-frequency χ , absolute frequency dependency of χ , and hard isothermal remanent magnetization) that may be used as proxies for pedogenic processes and paleoprecipitation, Wasiljeff et al. (2022) divided the Ulantatal dust sequence into four zones (Text S1 in Supporting Information S1), which we apply here to group the AMS data.

3.3. Detrital Zircon U-Pb Geochronology

Zircon dating was conducted at the GTK using the Analyte 193 ArF (Photon Machines, San Diego, USA) laser ablation system with the NuAttoM (Nu Instruments Ltd., Wrexham, UK) single collector inductively coupled plasma mass spectrometer (ICP-MS). Detailed instrumental parameters are presented in Table S1 in Supporting Information S1. The laser spot size was 15–25 μm depending on the grain size. Standard GJ-1 (609 ± 1 Ma; Horstwood et al., 2016; Jackson et al., 2004) was used for calibration, while in-house standards A382 ($1,877 \pm 2$ Ma) and A1772 ($2,711 \pm 1$ Ma; Huhma et al., 2012), and in some cases, Ple  ovice zircon standard (337 ± 1 Ma; Sl  ama et al., 2008), were used for quality control. A common lead correction after Stacey and Kramers (1975) was applied when $^{204}\text{Pb} > 100$ cps.

Similarity between samples was evaluated statistically through multidimensional scaling (MDS) using the R package “provenance” (Vermeesch et al., 2016). To quantitatively estimate the relative contribution of each selected source area to Ulantatal, we used the *DZmix* model by Sundell and Saylor (2017). *DZmix* implements an inverse Monte Carlo method to unmix the DZ age distribution. For the mixing calculations, we combined published secondary source area DZ U-Pb data (Bird et al., 2015; Bush et al., 2016; Che & Li, 2013; Kong et al., 2014; Licht, Pullen, et al., 2016; Nie et al., 2015; Pullen et al., 2011; Stevens et al., 2010, 2013; Xie et al., 2007; Yang et al., 2009; H. Zhang et al., 2016) to represent four distinct primary source regions: NTP (Qaidam, Qilian), North China Craton (NCC; East Mu Us, Mu Us Cretaceous sandstone, middle reaches of the Yellow River), central Central Asian Orogenic Belt (CAOB; Gobi-Altai Mts. piedmont, Tengger, and Badain Jaran), and eastern CAOB (central and southern Mongolia, Otindag and Horqin deserts). We applied 10,000 model trials, of which the best 1% were selected. Kernel density estimates (KDE; bandwidth: 20 Myr) were used as the comparison metrics for the cross-correlation of finite mixture distributions, and cumulative distributions for the Kuiper test *V* statistics, and Kolmogorov-Smirnov (KS) test *D* statistics.

3.4. Detrital Rutile Trace Elements

DRs were analyzed with the same laser ablation ICP-MS system as the DZ U-Pb ages (Table S1 in Supporting Information S1). The laser spot size was 15–25 μm . The standard BHVO-2G was used as an external standard, while BCR2-2G (Jochum et al., 2005; Schudel et al., 2015), R632 (Axelsson et al., 2018), and R10 (Luvizotto et al., 2009) were used for quality control. ^{47}Ti was used as an internal standard for rutile. 49 isotopes and 45 elements were measured. Data were processed using GlitterTM software (Van Achterberg et al., 2001).

For grains with Fe, Cr, V, Nb, Zr, and Sn contents above detection limits, rutiles were distinguished from other TiO_2 polymorphs using the spreadsheet by Triebold et al. (2011). Lithological discrimination based on Cr and Nb contents followed Triebold et al. (2012). Zr-in-rutile temperatures (ZiRs) were calculated following Tomkins et al. (2007) using the α -quartz setting. ZiR data from sedimentary source regions (Bohm et al., 2023b) were compared to the Ulantatal data.

3.5. Dust Modeling

To determine and compare the present-day source regions for Ulantatal and Baode, we performed backward simulations of silt-sized dust particles (described by a log-normal distribution varying between 15 and 20 μm) using the Lagrangian particle dispersion model FLEXPART v10.4 (Pisso et al., 2019). FLEXPART includes both wet and dry removal of particles, which are calculated in separate simulations. Our simulations were based on 3 hourly meteorological data from the ERA5 reanalysis with a $0.3^\circ \times 0.3^\circ$ resolution. Every three hours 50,000 (200,000) particles were released from the site location (Ulantatal, Baode) for the dry (wet) deposition calculations, after which they were traced backwards for 10 days. We ran FLEXPART for the main dust storm season from March to May over a 21-year period from 1999 to 2019. As the FLEXPART output consists of 3D fields of emission sensitivities, we took the emission sensitivity of the lowest 100 m and coupled it with dust emission fluxes from a FLEXDUST dust emission model (Groot Zwaafink et al., 2017). We used a version of FLEXDUST that contains several changes to better represent the East Asian dust cycle (Tang et al., 2023). By coupling the dust flux with the emission sensitivity, we obtained source contribution maps, which can be spatially integrated to give the dust deposition rate at the site. It should be noted that a major uncertainty inherent in this dust source contribution model is that the Paleogene paleogeography was different from today (Figure 1b). Moreover, comparing the modern dust cycle to that of the Paleogene is further complicated by the impact of human land use on dust emissions (e.g., S. Wang, Yu, et al., 2021).

4. Results

4.1. Anisotropy of Magnetic Susceptibility

4.1.1. AMS Parameters

The AMS zones based on Wasiljeff et al. (2022) were numbered here 1–4 (from oldest to youngest). Based on the values of P_j and F (Figure 2), Zone 4 was further divided into two sub-zones, 4a and 4b (threshold: 29 Ma). Zone 4b ($n = 75$) has the lowest mean P_j , F , T , and L of all the zones. Zone 4a ($n = 105$) has more variation in P_j and F than Zone 4b (Figure 2 and Figure S2 in Supporting Information S1). Zone 1 ($n = 10$) has the lowest χ and highest

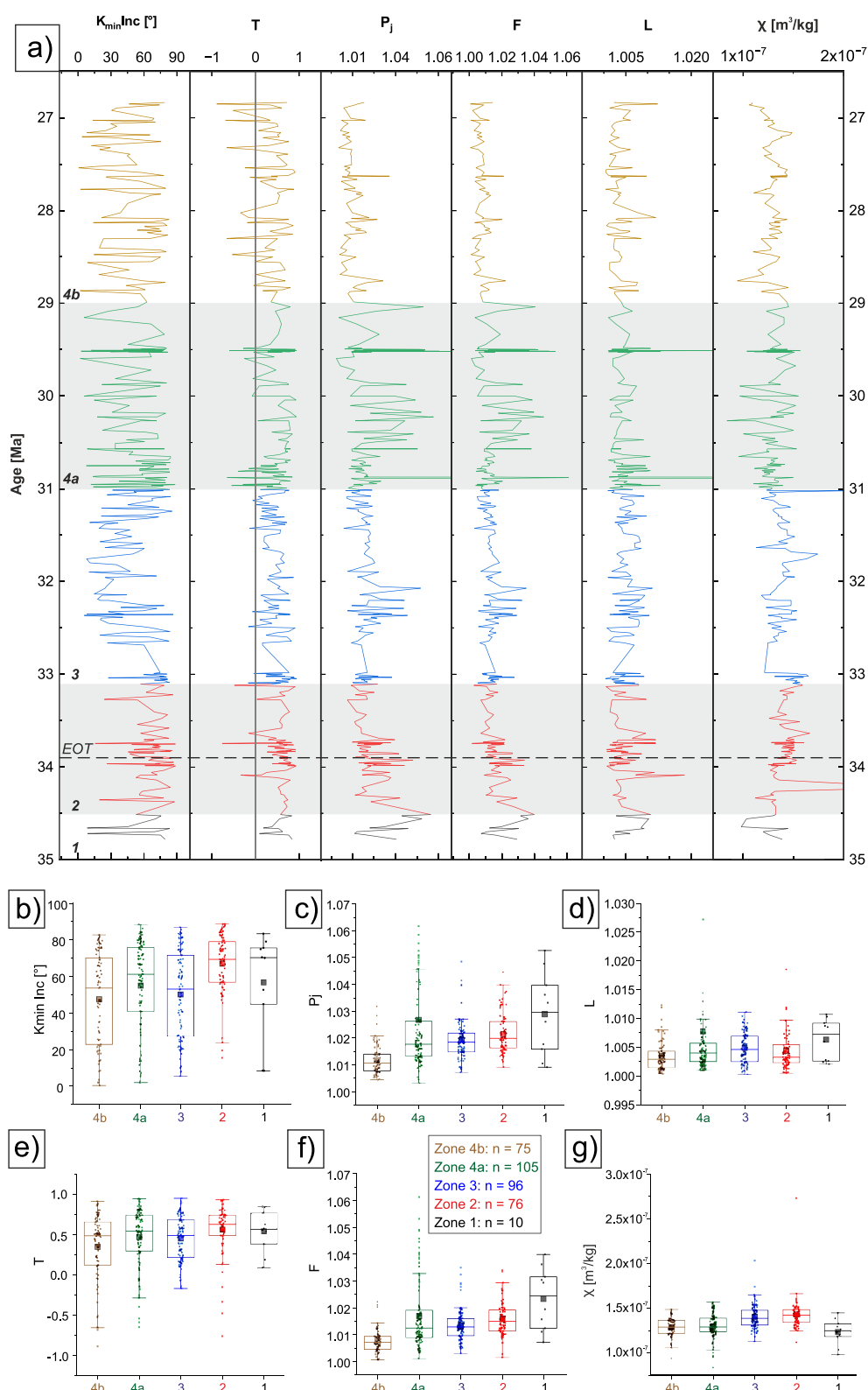


Figure 2. (a) Anisotropy of magnetic susceptibility (AMS) parameters versus depositional age. Colors and numbers in italics refer to the magnetic zones after Wasiljeff et al. (2022). The horizontal dashed line marks the Eocene-Oligocene transition. (b–g) Boxplots of AMS parameters. Numbers refer to the magnetic zones as in (a). Data points are plotted as circles. The boxes are the upper and lower quartiles of the data (width is irrelevant). Squares refer to the mean values, horizontal lines to median values. The whiskers represent ≤ 1.5 inter-quartile distance from the upper and lower quartiles.

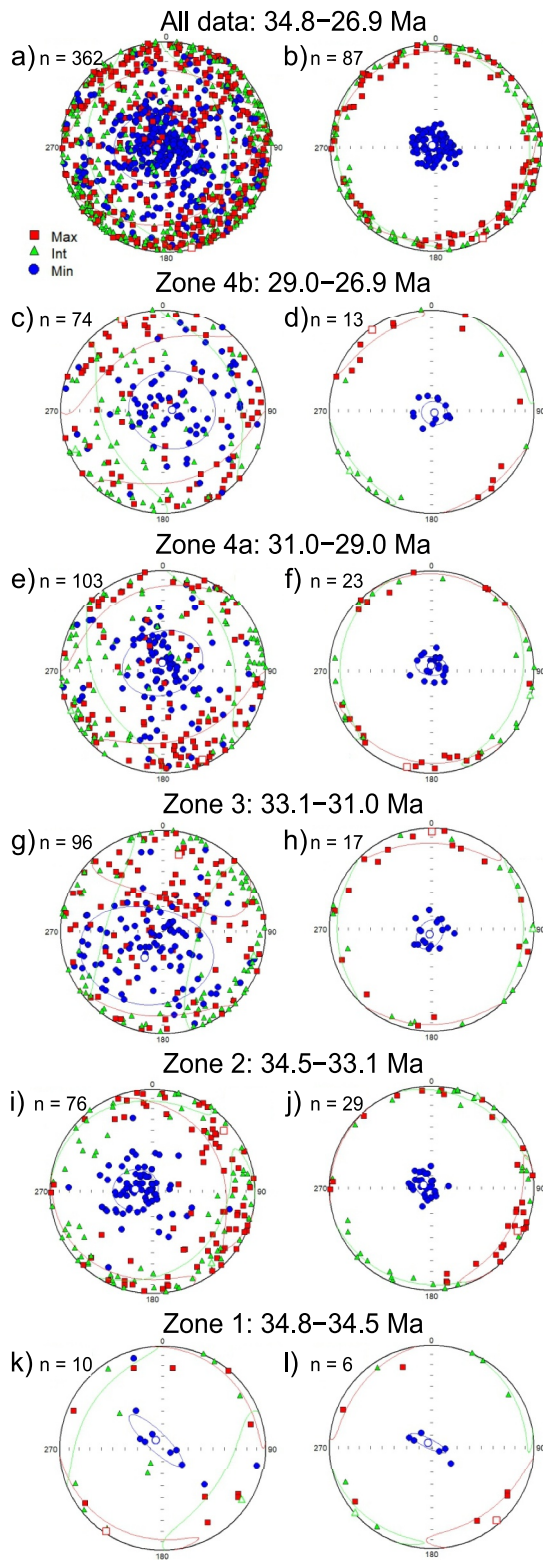


Figure 3. Anisotropy of magnetic susceptibility stereoplots of (a) all data, (b) all data with vertical K_{\min} , oblate shape, statistically significant foliation and lineation, and $F \gg L$, (c, d) the same for Zone 4b, (e, f) Zone 4a, (g, h) Zone 3, (i, j) Zone 2, (k, l) Zone 1.

mean F , L , and P_j (Figure 2), although these features could be explained by the small sample number compared to the other zones. Zones 2 ($n = 76$) and 3 ($n = 96$) have almost equally high χ , which then somewhat decreases in Zones 4a and 4b (Figure 2). Throughout the section, P_j and F have similar trends when plotted against depositional age (Figure 2a), confirming that F controls the shape of the AMS ellipsoid (Zhu et al., 2004). Overall, F is higher than L . The F – L diagram (Figure S2a in Supporting Information S1) and the positive values of T (Figure 2 and Figure S2e in Supporting Information S1) suggest that oblate shapes of the AMS ellipsoid are dominant throughout the section.

Based on E_{12} , F_{12} , and F_{23} , the majority of the samples have statistically significant magnetic lineations and foliations (Figure S2 in Supporting Information S1). The parameter E_{12} is the half-angle uncertainty of K_{\max} within the foliation plane, and predictably decreases as L increases (Figure S2d in Supporting Information S1). F_{12} and χ do not correlate (Figure S2g in Supporting Information S1), suggesting that random measurement errors are negligible (Zhu et al., 2004). In general, P_j and χ have no clear relationship (Figure S2h in Supporting Information S1).

4.1.2. Equal Area Projection Stereoplots

The mean tensors in the equal area projection of all analyses (Figures 3a and 3b) indicate steeply aligned K_{\min} and a shallow dipping K_{\max} , suggesting a quasi-horizontal depositional surface similar to field observations. The horizontally aligned magnetic lineations (K_{\max} axes) of all data are scattered. The K_{\max} mean tensor is oriented in the NW–SE direction.

Zone 1 (34.8–34.5 Ma) has a vertical mean K_{\min} and a horizontal mean K_{\max} in the SW direction (Figure 3k). After filtering out the measurements that most likely reflect secondary processes (Figures 3l), 60% of the MF of Zone 1 may represent a primary eolian MF, with a mean K_{\max} direction in the SE.

Zone 2 (34.5–33.1 Ma) has a steeply oriented mean K_{\min} , which is slightly imbricated to the fourth quadrant (Figure 3i). Mean K_{\max} correspondingly slightly deviates from the horizontal orientation with relatively scattered declinations. The filtered data (38%) clusters the K_{\max} declinations in the SE direction (Figure 3j).

Zone 3 (33.1–31.0 Ma) has several inverse MFs (vertical K_{\max}), and the mean tensor of K_{\min} is imbricated toward the third quadrant (Figure 3g). The filtered MF (18%; Figure 3h) shows scattered K_{\max} directions, with a mean tensor in the north.

Zone 4a (31.0–29.0 Ma) has a vertical mean K_{\min} and mean K_{\max} oriented in the SE direction (Figure 3e). However, there are also several inverse MFs. The filtered MF (22%; Figure 3f) shows K_{\max} directions in the NNW–SSE and SW–NE directions with a mean tensor in the SSW.

Zone 4b (29.0–26.9 Ma) has an overall stereoplot similar to Zone 4a, with a steeply dipping mean tensor of K_{\min} , and mean K_{\max} in the SE direction (Figure 3c). The filtered MF (18%; Figure 3d) has the most uniformly aligned K_{\max} axes of all units, with only three measurements deviating from the prominent NW–SE direction.

4.2. Detrital Zircon U–Pb Geochronology

The DZ ages are mostly in the ranges 300–200 and 500–400 Ma (Figure 4). Minor age peaks occur at 1,000–500, c. 1,800, and c. 2,500 Ma. Most notable

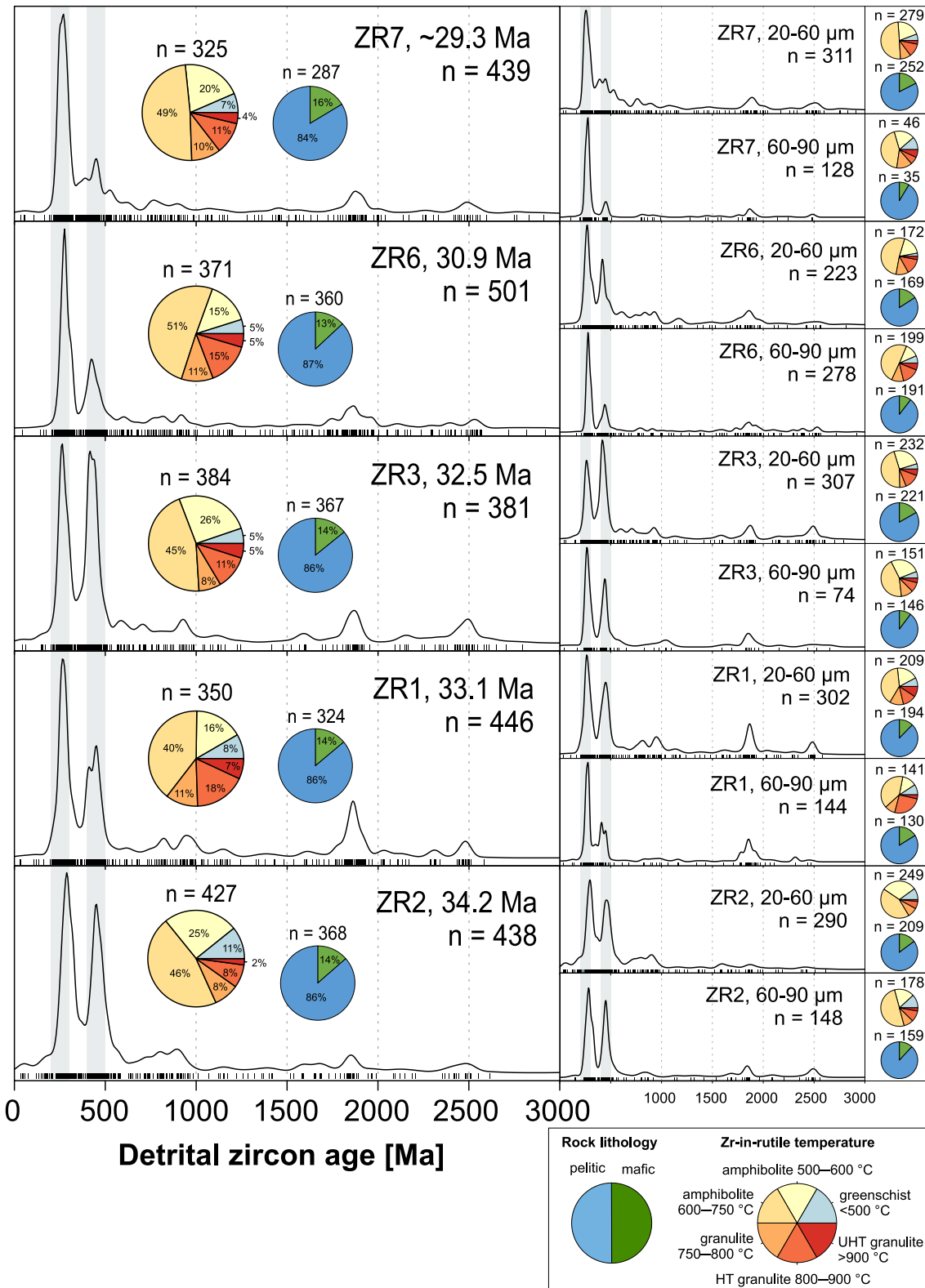


Figure 4. Kernel density estimates (adaptive bandwidth) of the detrital zircon ages and pie charts of the Zr-in-rutile temperatures and Cr-Nb lithology discrimination of detrital rutile data. The same data are divided into the finer and coarser grain size fractions on the right-hand side. Gray bars indicate the time intervals 500–400 Ma and 300–200 Ma. HT = high-temperature, UHT = ultrahigh-temperature.

intersample differences are in the proportions of the age ranges 300–250 and 450–400 Ma, while smaller but notable variations are also seen in the 250–200, 500–450, and 2,500–1,600 Ma (Paleoproterozoic) age range proportions (Figure S3 in Supporting Information S1). The number of Mesoproterozoic DZs is generally low.

A notable grain size effect is seen in the proportions of the age ranges 300–250 Ma [coarser, 60–90 μm , fraction has a higher proportion (22%–45%) than the finer, 20–60 μm , fraction (14%–19%) in all samples] and 1,000–541 Ma [Neoproterozoic; finer fraction has a higher proportion (14%–19%) than the coarser fraction (5%–8%) in all samples] (Figure S3 in Supporting Information S1). Although the grain size effects could result from the generally lower analysis numbers on the coarser fraction, almost equal sample sizes of the finer and coarser fractions in sample ZR6 (30.9 Ma) suggest they are not a function of sample size. ZR6, ZR1 (33.1 Ma), and ZR2 (34.2 Ma) have slightly elevated proportions of Paleoproterozoic zircons in the coarser fraction. The most pronounced grain size effect in the age distributions is in the two youngest samples (ZR6; 30.9 Ma and ZR7; \sim 29.3 Ma). The Neoproterozoic ages in the fine fractions differ between samples. In ZR2, the ages are mostly 600–541, 950–850, and 800–700 Ma. In ZR1, most are 1,000–950 and 850–800 Ma. ZR3 (32.5 Ma) and ZR6 have more widely distributed Neoproterozoic ages, but 1,000–950 Ma ages are low in number. ZR7 has mostly 650–541 Ma zircons and a small number of early Neoproterozoic zircons.

Sample ZR1 (33.1 Ma) has one DZ age, 31.895 ± 0.750 Ma, younger than the depositional age. Considering the uncertainty, and the fact that a small Pb loss can result in a slightly younger age than the real crystallization age, this DZ age can be considered approximately coeval with the depositional age.

In the MDS plot, ZR3 (32.5 Ma) is the only sample that plots closest to the NTP (Figure 5a). However, when divided into finer (20–60 μm) and coarser (60–90 μm) grain size fractions, both ZR3 and ZR1 (33.1 Ma) plotted close to the NTP in the finer fractions (Figure 5b). Finer fractions of ZR6 (30.9 Ma) and ZR2 (34.2 Ma) also plot close to the ZR3 and ZR1 fine fractions. All coarser fractions plot closer to the CAOB. None of the samples appear closely affiliated with the NCC.

When considering all grain sizes, the results of the *DZmix* model are consistent between the cross-correlation, Kuiper and KS statistics for all Ulanatal samples except the ZR2 (34.2 Ma) sample. The cross-correlation of KDEs was chosen for the quantitative estimation of source contributions to the Ulanatal dust sequence, as it generally had lower standard deviations than the Kuiper test *V* or KS test *D* statistics and its results are consistent with the MDS. The cross-correlation values for the different calculations were ≥ 0.89 , indicating good fits of the data. The oldest sample, ZR2, has 56% contribution from the central CAOB and 36% from NTP (Figure 5g). Samples ZR1 (33.1 Ma) and ZR3 (32.5 Ma) show the highest contribution from the NTP (37% and 63%, respectively). ZR1 also has a major contribution from the central (28%) and eastern (22%) CAOB, while in the ZR3 sample, those contributions are lower, 19% and 13%, respectively. NCC also contributes 14% to the 33.1 Ma age distribution. The youngest units, ZR6 (30.9 Ma) and ZR7 (\sim 29.3 Ma), have the largest contribution from the central (85% and 44%, respectively) or eastern (48% for the \sim 29.3 Ma sample) CAOB with low contributions ($<5\%$) from the NTP.

When the finer and coarser grain sizes are separated for the mixing calculations, the consistency between the different statistical methods decreases, possibly caused by the decreased sample sizes. Despite this, the cross-correlation values remain above 0.84, indicating good fits of the data. All coarser grain size fractions show the highest relative contributions from the central CAOB (38%–87%; Figure 5g). NTP contributions were higher in the finer fraction than in the coarser fraction in all samples. The two youngest units show a NTP contribution essentially only in the finer grain sizes.

4.3. Detrital Rutile Trace Elements

The Cr and Nb contents in each DR sample define 84%–87% of the rutiles as metapelitic in lithology (Figure 4). Excluding ZR1 (33.1 Ma), all samples had higher proportions of metamafic rutiles in the finer than coarser fractions. However, in ZR7 (\sim 29.3 Ma), the small number of analyses from coarse grains may limit comparisons. Based on ZIR, ZR7 contains 25% granulitic rutiles, ZR6 (30.9 Ma) 31%, ZR3 (32.5 Ma) 24%, ZR1 36%, and ZR2 (34.2 Ma) 18%. ZR1 shows a notable grain size effect: the finer fraction has 12% high-temperature granulite facies rutiles, while the coarser fraction has 26%. The ZR2 finer fraction shows a higher proportion (31%) of low amphibolite facies rutiles than the coarser fraction (17%). The MDS of the ZIR data reveals that most Ulanatal samples plot close to each other (Figure 5c), except samples ZR1 and ZR6. The coarser fraction of ZR1 is the

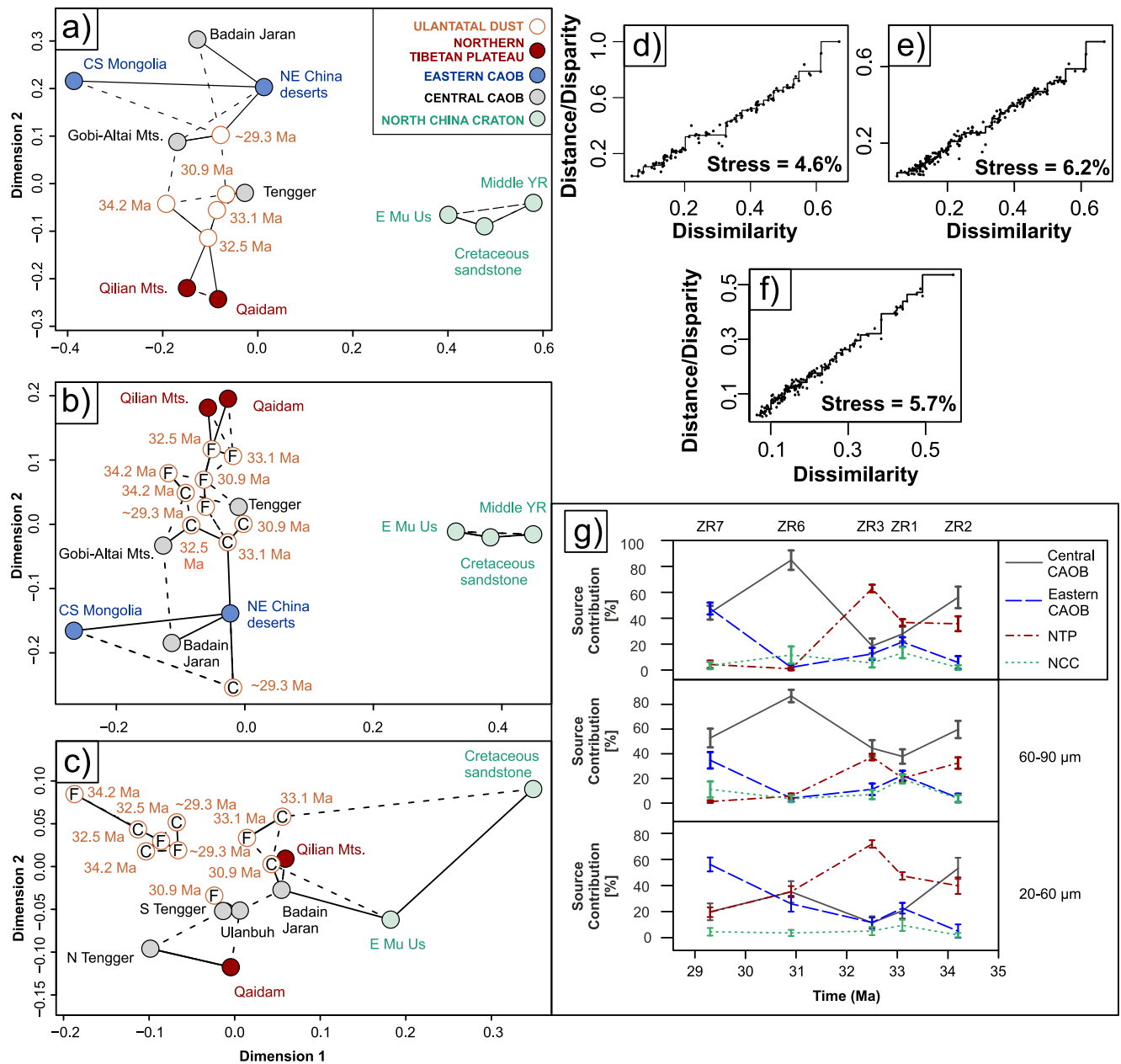


Figure 5. Multidimensional scaling plots of (a) detrital zircon (DZ) ages, (b) DZ ages with Ulanatatal samples divided into finer (F; 20–60 μm) and coarser (C; 60–90 μm) grain size fractions, and (c) ZrR data with Ulanatatal samples divided into the same grain size fractions as in (b). Panels (d–f) are the Shepard plots for the MDS plots in (a–c), respectively. (g) Results from the *DZmix* model (Sundell & Saylor, 2017) cross-correlation for all data (top) and the grain size fractions (middle and bottom).

second closest sample to the Cretaceous sandstone. The coarser ZR6 fraction plots closest to Qilian and Badain Jaran, while the finer fraction lies closest to South Tengger.

5. Discussion

5.1. General Provenance Trends and Applicability of ZrR in Sourcing Ulanatatal Dust

The high DZ age peaks at 300–200 Ma and the *DZmix* model results indicate dominant CAOB sources to the north/northwest of Ulanatatal for the oldest sample (34.2 Ma) and the two youngest samples (30.9 and ~29.3 Ma; Figures 4, 5g, 6c). In the *DZmix* model, the finer fractions of the two youngest samples also have relatively high amounts of eastern CAOB source input, while the oldest sample exhibits minimal input from any easterly sources

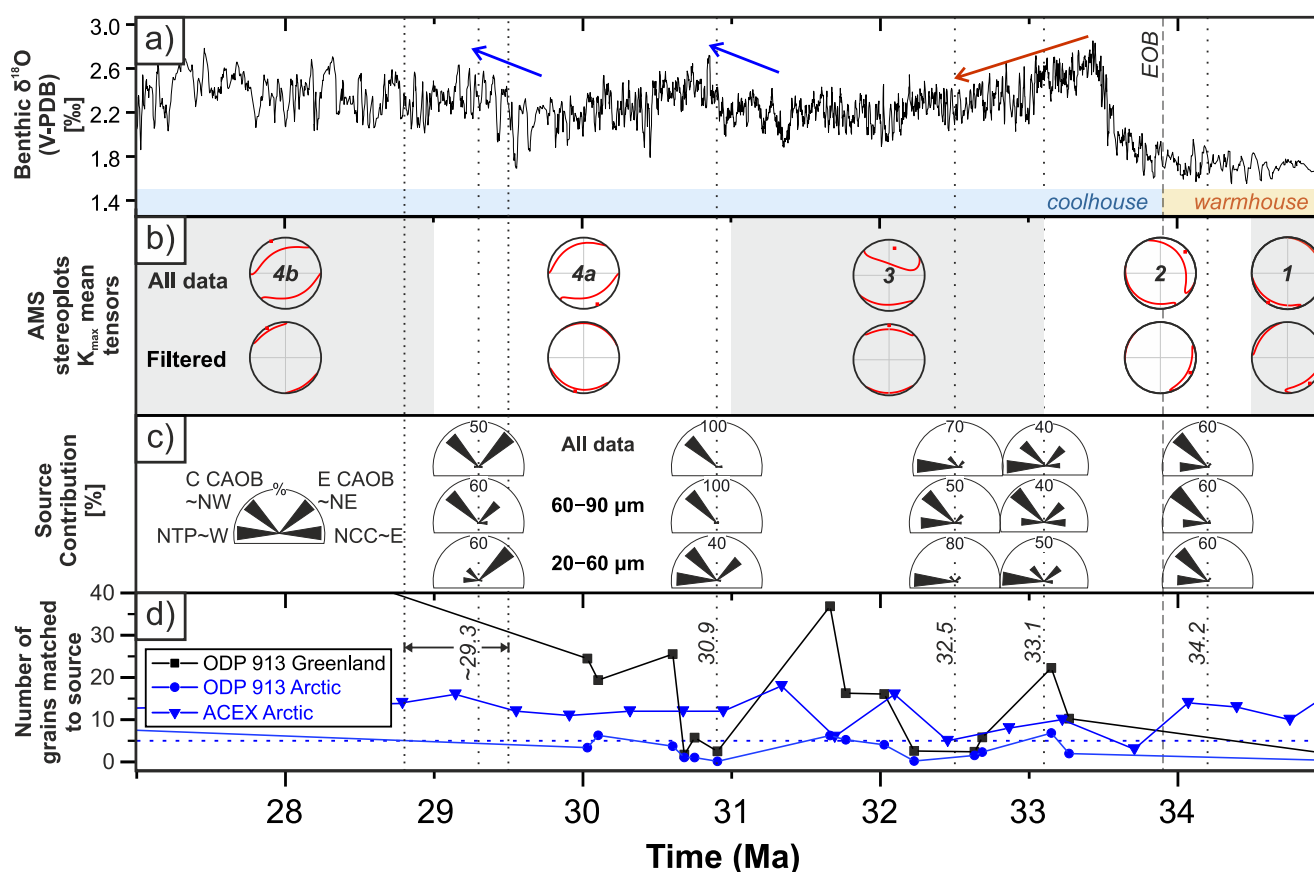


Figure 6. (a) Oxygen isotopes from benthic foraminifera (five-point running mean) from Tripati and Darby (2018) and references therein. Blue (red) arrows indicate a cooling (warming) trend in the Oligocene. (b) simplified anisotropy of magnetic susceptibility stereoplots showing only the mean tensors of the K_{max} axes (magnetic lineation) for each magnetic zone discussed in the text, (c) results from the cross-correlation of the *DZmix* model (Sundell & Saylor, 2017) for Ullatatal detrital zircon age data plotted as rose diagrams, and (d) numbers of Fe oxide grains matched with Arctic (blue) or Greenland (black) sources from ice-rafted debris in Greenland Sea (ODP 913) and central Arctic Ocean (ACEX site). The blue dashed line refers to five grains matched to Arctic sources (threshold for highly significant influx of ice-rafted Fe oxide grains). According to Tripati and Darby (2018), the grains from Arctic sources were likely transported by sea ice, while the grains from Greenland were likely derived from glacial ice via icebergs. Data are from Tripati and Darby (2018) and references therein. EOB = Eocene-Oligocene boundary.

(E CAOB and NCC; Figures 5g and 6c). Based on the *DZmix* model, all samples exhibit some source input from the NTP to the west, which in the youngest samples is limited to the finer grain sizes (Figures 5g and 6c). The 33.1 and 32.5 Ma samples are dominantly sourced from the NTP, as also indicated in the high proportions of 500–400 Ma DZs, especially in the 32.5 Ma sample (Figure 4). The 33.1 Ma sample has an additional source component from the NCC, which is specifically expressed by the Proterozoic and Archean DZ ages and the high proportion of granulite-facies DRs (Figure 4), which suggest origin from the Khondalite Belt (NCC) to the east of Ullatatal, of which the Helan Mts. are also part (Figures 1d and 5g; Bohm et al., 2022). Both the 33.1 Ma and 32.5 Ma samples also have significant contributions from the CAOB sources, especially in their coarse fractions (Figures 5g and 6c).

Intersample variation in the Ullatatal ZIR data is small. The DR data are only critical for provenance inferences in confirming the NCC source contribution from the east to the 33.1 Ma sample. The low intersample variability in the ZIR temperatures may be explained by the fact that potential source areas with very low or very high metamorphic temperatures are not present for Ullatatal (exception is the 33.1 Ma sample), as such areas lie well to the east of Ullatatal (Khondalite Belt and Trans-North China Orogen: high temperatures; Bohm et al., 2022), were partly or completely covered by the Paratethys Sea (Q. Li et al., 2020), or only uplifted in the Miocene (J. Sun et al., 2022 and references therein), and thus not active silt producing regions in the Paleogene (Junggar and Tianshan: low temperatures; Bohm et al., 2022). For these reasons, the Ullatatal ZIR results concentrate on amphibolite facies, the most common facies for rutile formation generally and in the source areas overall (Bohm et al., 2022). The only dominantly low-temperature terrane able to produce silt in the Paleogene would have been

North Qilian (Bohm et al., 2022). Indeed, the NTP-source dominated 34.2 Ma finer fraction has a higher proportion (31%) of low amphibolite facies DRs than the coarser fraction (17%), supporting the above conclusions as finer grain sizes are more likely transported over longer distances from the NTP. However, the sedimentary sample of Qilian does not reflect the North Qilian low-temperature primary rocks (Bohm et al., 2023a), which, in addition to the issues mentioned above, is one of the reasons why the MDS of ZiRs (Figure 5c) is not considered diagnostic of the Ulantatal provenance.

5.2. AMS Inferred Surface Wind Strength and Directions

The maximum saturation magnetization value in the Ulantatal dust sequence is $0.029 \text{ A.m.}^2 \text{ kg}^{-1}$ (Wasiljeff et al., 2022), which corresponds to 0.03 wt.% of magnetite. Magnetite will dominate the AMS if magnetite content exceeds $\sim 0.7 \text{ wt.}\%$ (Lagroix & Borradaile, 2000; Taylor & Lagroix, 2015). The low magnetite content and the overall weak bulk χ values of the Ulantatal Formation indicate that the AMS is dominated by paramagnetic minerals, consistent with the lack of a clear relationship between P_j and χ (Figure S2h in Supporting Information S1; Borradaile, 1987; Hus, 2003; Rochette et al., 1992). The most common paramagnetic minerals in the Ulantatal dust sequence are phyllosilicates (Wasiljeff et al., 2022), which show intrinsically oblate AMS character.

The oblate shapes of the Ulantatal AMS ellipsoids are typical features of loess deposits and are commonly related to the dominance of phyllosilicates and gravitational depositional environments (e.g., Bradák et al., 2020; Kölltringer et al., 2021; Lagroix & Banerjee, 2002; Taylor & Lagroix, 2015; Zhu et al., 2004). Many Ulantatal samples have non-vertical K_{\min} inclination and, in general, comparatively scattered AMS ellipsoid orientations. MF deviating from the most likely primary eolian MF identified from the data based on the criteria in Section 3.2 may point to partial reworking, strong winds, or deposition on a slope (Nawrocki et al., 2006; Tarling & Hrouda, 1993). As the Ulantatal AMS samples were collected from quasi-horizontal surfaces, any imbrication is unlikely to be created by the slope deposition. Reworking features are likely caused by the relatively low χ and the relative age of the sediments (compared to Quaternary loess which have been the subject of most AMS studies on loess). The potentially longer time interval for the dust deposits here to be subjected to post-depositional processes and to secondary magnetic mineral formation would lead to an increased likelihood of disturbance to the primary eolian MF.

The stereoplot for specimens of all samples (34.8–26.9 Ma) after filtering (Figure 3b) shows scattered declinations of the K_{\max} axes, indicative of a gravitation-aligned MF. However, the very weak alignment of K_{\max} in the NW-SE direction may indicate the overall prevailing wind direction. The relatively weak anisotropy suggests that the overall wind strength was likely weak, that multiple prevailing surface wind directions were present, or that the prevailing surface wind directions have changed over time in the Ulantatal dust sequence. As such, each magnetic zone is therefore discussed separately.

The high P_j of Zone 1 (34.8–34.5 Ma; Figure 2) suggests a relatively high-energy sedimentary environment. However, the number of data points is lower than in the other zones, increasing the uncertainty and hampering any paleowind inferences. The stereoplot of all data (Figure 3k) indicates a gravitational or weakly flow-aligned MF in the SW-NE direction. After data filtering (Figure 3l), the mean K_{\max} suggests NW-SE oriented paleowinds (Figures 3l and 6b). Combined, the high P_j and the relatively clear flow direction may indicate relatively strong winds along the NW-SE orientation.

The unfiltered data of Zone 2 (34.5–33.1 Ma; Figure 3i) indicate an imbricated fabric in the (N)W direction, which may be produced by primary eolian deposition or by post-depositional processes. Overall, the imbrication suggests an easterly wind component, which is consistent with the provenance data. The mean K_{\max} of the filtered data (Figure 3j) suggests NW-SE oriented paleowinds, similar to Zone 1, but the weak imbrication of K_{\min} axes to the NW persists. The filtered mean K_{\max} direction, however, differs $\sim 90^\circ$ from that of the whole data of Zone 2. If created by wind, the imbrication of the mean K_{\min} to the (N)W suggests a dominant paleowind direction from the (south)east if weak winds or (north)east if strong winds (Nawrocki et al., 2006; Tarling & Hrouda, 1993). The allocation of weak versus strong winds to south- versus northeast is not very clear because the imbrication direction is only very slightly in the NW and the K_{\max} directions are relatively scattered. The imbrication may also indicate relatively weak northeasterly (mean K_{\max} direction) prevailing surface winds that re-orientate grains after deposition but before burial (“transformed MF”; Bradák et al., 2018; Nawrocki et al., 2006). However, if only the filtered data are considered, such winds would be southeasterly. Transformed MF is favored when sedimentation

rates are low, which is consistent with Zone 2 (~10 cm/kyr; Wasiljeff et al., 2020), although similar rates (~11 cm/kyr) are calculated also for the upper levels of the Ulanatal sequence. As such, the MF of Zone 2 was possibly created by weak southeasterly winds that produced a transformed MF after deposition, although the overall direction of lineation may also indicate northeasterly winds. Importantly, an easterly source contribution is consistent with the source inferences from the DZ and ZiR data (Section 5.1). Although the EOT did not have an effect on the paleoprecipitation proxies in Ulanatal (Wasiljeff et al., 2022) nor to the AMS parameters of this study (Figure 2), the easterly component indicated by the MF in Zone 2 and the post-EOT (33.1 Ma) DZ and DR data, was perhaps introduced as a response to the EOT, as such components are minimal in the Eocene 34.2 Ma sample (Figures 5g and 6c). Although the inferred 33.1 Ma provenance may also be related to possible minor uplift of Helan Mts. poorly constrained at c. 30 Ma (Zhao et al., 2007), the addition of an easterly wind component at the EOT could reflect the instability or reorganization of Asian atmospheric circulation as a response to the major global climate transition.

The imbricated MF of Zone 3 (33.1–31.0 Ma; Figure 3g) could be interpreted to represent a northeasterly paleowind direction based on the same reasoning as for Zone 2. However, the mean tensors are not as well constrained as in Zone 2, which may point to reworking, especially as the filtering removes 82% of the data. The mean K_{\max} alignment in the filtered data (Figure 3h) implies the N-S flow direction but the scattering of the K_{\max} axes indicates a gravitational settling control and therefore, weaker surface wind strengths during this time. Paleoclimate proxies suggest increased aridity in Ulanatal during deposition of Zone 3 culminating in the EOAE at 31 Ma (Wasiljeff et al., 2022). The DZ data reveal a dominant westerly source input from the NTP at 32.5 Ma (Figures 5a, 5b, 5g, and 6c), which is inconsistent with the possible N-S surface wind direction indicated by the AMS. The reasons for this inconsistency are unclear, but further support the inference of reworked sediments. Because of the increasing aridity, the signs of reworking, such as multiple specimens showing an inverse MF, are interpreted to be caused by postdepositional mechanical processes (e.g., desiccation cracks) rather than pedogenesis, despite the relatively high χ of the zone. A transformed MF is also feasible for this zone, as prolate single-domain magnetite grains (producing the high χ) aligned parallel to the wind direction on a horizontal depositional surface would have steep K_{\max} directions (inverse MF).

The MF of Zones 4a–b (31.0–26.9 Ma) shows a vertical mean K_{\min} , and slightly clearer flow directions in the NW-SE and SW-NE directions, as indicated by the clustered K_{\max} directions (Figures 3c–3f), especially in Zone 4b (Figures 3c and 3d). The sedimentary environment, and possibly paleowinds may have thus become more consistent after the EOAE. Combined with the DZ results that indicate the source contribution mostly from the CAO (Figures 5g and 6c), northwesterly dust transporting winds likely dominated during this time. This may indicate a stabilization, or possibly strengthening, of northerly/northwesterly winds at c. 31 Ma. Interestingly, the two major magnetic lineation directions (NNW-SSE and SW-NE) of Zone 4a could also reflect an MF created by the combination of dust transporting northerly/northwesterly winds and moisture transporting southwesterly winds. The studies of Zhu et al. (2004) and R. Zhang et al. (2010) from Quaternary loess on the CLP suggest that summer monsoon winds and rains reorient the EAWM-transported grains and align newly formed magnetic particles in its direction (NW-SE in the CLP). Following this line of argument, moisture-transporting southwesterly winds at Ulanatal could also explain the observed SW-NE direction of lineation in Zone 4a and to a lesser degree in Zone 4b. This would be consistent with Wasiljeff et al. (2022) who reported higher precipitation for Ulanatal after 31 Ma (which corresponds with Zone 4a) and favored the westerly winds over the summer monsoon as the moisture source.

5.3. Paleogene Wind Regime and the Role of Paleogeography in the Long-Term Dust Cycle

In contrast to the AMS results, the detrital mineral analyses provide information on wider dust transporting wind systems than only the surface winds at the sample site. As expected (Pye, 1987), the coarser grain size fractions of all samples reflect more proximal source regions of the central CAO (Figures 5b and g). However, a NTP source is also suggested in the coarser fractions of the 32.5 Ma and older samples (Figure 5g), confirming that this westerly source input (whether stepwise or direct wind transport) is not restricted to the finer grain sizes. As the younger samples also have notable proportions of NTP-sourced DZs in their finer fractions, westerly winds likely transported dust to Ulanatal throughout the phase of dust deposition recorded at Ulanatal. However, northerly/northwesterly/northeasterly winds from the (central and eastern) CAO dominate the provenance in the oldest and youngest samples, and notably also contribute to the NTP-dominated 33.1 and 32.5 Ma samples. Thus, we conclude that overall Paleogene atmospheric circulation in the wider area exhibits strong westerly and northerly/

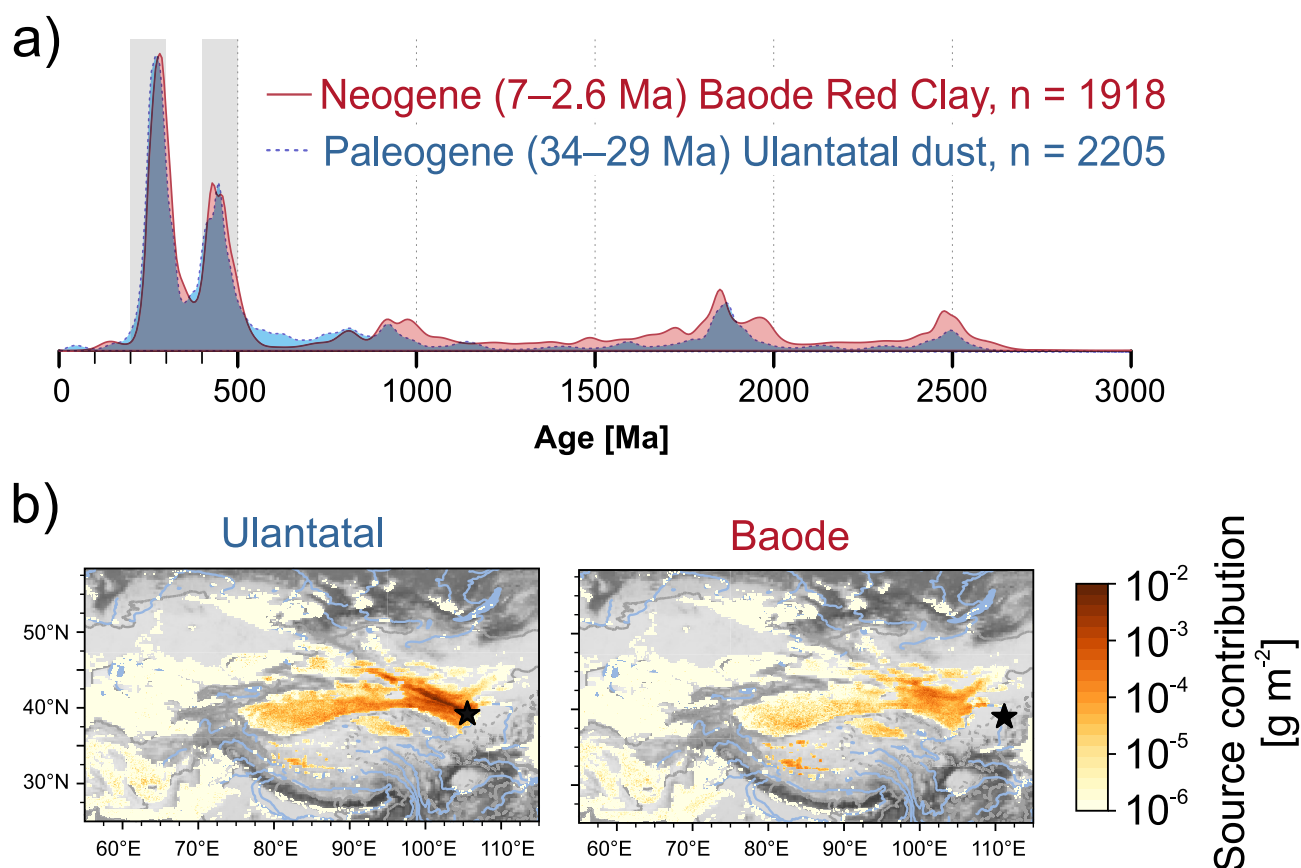


Figure 7. (a) Kernel density estimates (adaptive bandwidth) of combined detrital zircon age data sets from Ulanatal (this study) and Baode (Bohm et al., 2023b; Shang et al., 2016). (b) Average source contribution of total deposition (wet + dry) at Baode and Ulanatal. Stars indicate the locations of the sites.

northwesterly components, which is strikingly similar to that of the late Neogene-Quaternary (e.g., Shang et al., 2016; H. Zhang et al., 2022). To further test the similarity of the Paleogene circulation patterns to those of the Neogene-Quaternary, we compared the Ulanatal DZ provenance signal to that of Baode Red Clay (Bohm et al., 2023a, 2023b; Shang et al., 2016) and modeled the modern-day dust source contributions to these sites by combining backward particle dispersion and dust emission models (Figure 7). Baode is located on the same latitude as the Ulanatal site ($\sim 40^\circ\text{N}$), and therefore is likely to be influenced by similar wind systems, if they were present. Indeed, the DZ age distributions of the combined Ulanatal and Baode sites are almost identical, and the source contribution model shows that they are influenced by approximately the same sources (Figure 7). For comparison with a wider coverage of the northern CLP, we have also combined the Baode DZ data with those from the Jiaxian (W. Peng et al., 2023; H. Zhang et al., 2022) in Figure S4 in Supporting Information S1. Given that the major paleogeographic differences between the Paleogene and late Neogene Asia are related to the position and height of the TP, and the extent of the Paratethys Sea, our finding implies that the evolution of these features had little effect on the Central-East Asian dust cycle and atmospheric dust transport over million-year time scales (Licht, Dupont-Nivet, et al., 2016; Pan et al., 2023). Although the paleolatitude of the Ulanatal site at 30 Ma (Figure 1b) indicates that the site was located slightly ($\sim 3^\circ$) further north than today, the difference is small when considering the wider atmospheric circulation.

5.4. Drivers of Paleogene Dust Provenance

The long-term stability of dust provenance raises the question of what caused the Ulanatal dust sequence to form under seemingly similar atmospheric circulation conditions as today, but during significantly higher global temperatures. The loess formation requires an active dust source, a consistent transport pathway, and depositional conditions that permit trapping and preservation of wind-deposited sediments. A stable depositor occurred at least throughout the deposition of the sequence at Ulanatal. The existence of Paleogene

dust deposits suggests that silt production in Central Asia sufficient for loess formation occurred before the EOT (Abels et al., 2011; J. X. Li et al., 2018; X. Li et al., 2018b; Licht, Dupont-Nivet, et al., 2016; Wasiljeff et al., 2020), implying sufficient aridity and/or high mountain silt production. Here we argue that aridity was the main mechanism for silt production in the Paleogene, as most regions in CAO were uplifted only in the Miocene (J. Sun et al., 2022 and references therein), and the TP was likely lower and/or more topographically variable than in the Neogene (e.g., Fang et al., 2020; Spicer et al., 2020; Su et al., 2019), limiting the amount of Paleogene high mountain erosion. Increased fluvial activity has also been argued to influence the Neogene-Quaternary CLP dust provenance through enhanced silt availability in, for example, alluvial fans and floodplains (e.g., W. Peng et al., 2023; J. Sun et al., 2022). However, compared to the Neogene-Quaternary, the fluvial systems of the Paleogene are poorly constrained, and because of the lower elevation, it is likely that Paleogene fluvial erosion and comminution in the potential dust source regions were less intense, and alluvial fans were smaller in size and lower in number than in the Neogene-Quaternary. Although the lack of detailed reconstructions of Paleogene fluvial systems leaves some uncertainty in our provenance inferences, we argue that, contrary to the Neogene-Quaternary, changes in dust production in the source areas by large fluvial systems is an unlikely explanation for the observed provenance changes in Ulanat. Instead, our current view is that Ulanat dust provenance variations are mostly explained by changes in the wider atmospheric circulation patterns and dust transporting winds.

It is also unlikely that regional climate changes controlled the Ulanat dust provenance. Paleoclimate proxies reported by Wasiljeff et al. (2022) for the Ulanat sequence do not indicate any regional climate changes at the EOT, despite the dust provenance shift observed in this study. In fact, Wasiljeff et al. (2022) suggest a stable arid regime in Ulanat until c. 31 Ma, after which their data indicate environmental instability. In contrast, the AMS and provenance data here suggest most “stable” northwesterly winds (i.e., mostly only northwesterly and/or northeasterly source/surface wind components consistent with strong SH—see the following paragraphs) at the AMS Zones 4a and 4b (i.e., after 31 Ma) and in the youngest DZ sample at ~29.3 Ma. This inconsistency between the combined AMS and provenance data compared to the Ulanat climatic proxies strongly suggests global, rather than regional, control of the Ulanat dust provenance.

Neogene-Quaternary CLP dust formation and transport are widely believed to be dominantly controlled by northwesterly winds primarily driven or enhanced by the EAWM, in turn coupled to SH strength, itself linked to global climate evolution (e.g., Bohm et al., 2023a; Lu et al., 2010; H. Zhang et al., 2022) and the occurrence of NH ice sheets since at least the middle-late Miocene (e.g., Helland & Holmes, 1997; Krissek, 1995; Larsen et al., 1994). Based on our results, we propose that global cooling, and specifically, increased Paleogene NH ice volume, also largely controlled Ulanat dust provenance. Ice-rafted debris (IRD) and ocean chemistry evidence show indications of Eocene-Oligocene Arctic sea ice and minor NH continental ice (Coxall et al., 2005; Eldrett et al., 2007; Moran et al., 2006; Tripathi et al., 2005), which was likely ephemeral in the Eocene and only stabilized in the earliest Oligocene (Tripathi & Darby, 2018), coinciding with the onset of eolian dust deposition at Ulanat from the latest Eocene. Although the existence of extensive Eocene-Oligocene NH ice sheets is debated (e.g., Edgar et al., 2007; Spray et al., 2019), glacial ice in eastern Greenland coupled with Arctic sea ice (Tripathi & Darby, 2018) may have been sufficient to impact Asian atmospheric circulation.

When compared with the IRD records from the Arctic region (Tripathi & Darby, 2018), the Ulanat provenance results in Figure 6 show that during periods of less extensive NH polar ice (IRD), corresponding to the DZ samples at 34.2 Ma [deduced from the warmhouse climate conditions and the zero IRD values in the Tripathi and Darby (2018) data at 35.4 Ma], 32.5 Ma, and 30.9 Ma, contributions from the easterly dust sources (E CAO and NCC) are relatively low (except in the finer fraction of 30.9 Ma sample). In the only Eocene sample, the easterly component is essentially lacking. The only atmospheric system in the study region able to produce northeasterly/easterly dust transporting winds is the anticyclonic SH (Figure 1a). These easterly/northeasterly winds are weaker than the northwesterly winds and would not in any case be responsible for the bulk of dust transport, consistent with our results. Given its location, Ulanat is an ideal site to detect this easterly/northeasterly wind component, which essentially may be used as a proxy for the SH. Our results show the first clear sign of an easterly source component in the 33.1 Ma sample, implying that the SH either formed or strengthened after the EOT or was located more northward in the Eocene. Thus, the likely absence/reduced strength of the SH means it could not have been responsible for the northwesterly source component (C CAO) of the Eocene 34.2 Ma sample (Figure 6c). Instead, we suggest that the Eocene warmhouse conditions favored long-term negative AO-like conditions, resulting in a meandering pattern of planetary westerly circulation in the NH (Figure 1a). Such a

wave-like wind pattern would have had a northwesterly pathway in its descending limb, resulting in the mixed NTP-C CAOB (~W-NW) provenance observed in the Eocene sample.

After the EOT, dust provenance data suggest both the existence of the SH, but also strong westerly dust input from the NTP in the 33.1 and 32.5 Ma samples (Figures 5 and 6c). The 33.1 Ma sample is the only sample in our record where the provenance signal may suggest an influence of tectonically enhanced silt production in the source areas. First, the coeval DZ with deposition, which is more likely sourced from the potassic-adakitic Oligocene magmatism in the TP (Ding et al., 2003; Kapp & DeCelles, 2019) than from basaltic c. 33 Ma (Ar-Ar; Barry et al., 2003) volcanism in Mongolia, may indicate increased silt production on the NTP. Furthermore, the NCC source component of the 33.1 Ma sample may indicate increased erosion as a result of the poorly constrained c. 30 Ma Helan Mts. uplift (Zhao et al., 2007). However, by this point global climate had transitioned to a coolhouse state, which we argue also meant a shift from long-term negative AO-like conditions to long-term positive AO-like conditions, resulting in stronger and more zonal westerly winds. When compared to the following 32.5 Ma sample, the NH ice volume increase approximately coeval to the 33.1 Ma sample (Figure 6) may have also meant a stronger SH, and therefore a greater northerly (northeasterly and northwesterly) source component (E CAOB and C CAOB) in the 33.1 Ma sample. Toward 32.5 Ma, global climate warmed somewhat (Figure 6a), and NH ice volume decreased (Figure 6d), possibly resulting in relative weakening of the SH, thus driving the observed decrease in northerly source input to the 32.5 Ma sample. However, compared to the Eocene 34.2 Ma sample, the climate at 32.5 Ma was significantly cooler, allowing more positive AO-like conditions and stronger zonal westerly wind dust transport. To summarize, the general differences in global temperatures between 33.1 and 32.5 Ma, and possibly, in the extent of NH polar ice, modulate the SH strength and the dust provenance.

The following sample at 30.9 Ma, similar to the 32.5 Ma sample, was deposited at a time of decreased NH ice volume, as suggested by the IRD records, but shows a more dominant northerly (C CAOB and E CAOB) than westerly (NTP) source contribution (Figure 6). However, in contrast to the 32.5 Ma sample, the 30.9 Ma sample was deposited during a global cooling trend (Figure 6a). Thus, northerly dust transport may reflect the onset of a strengthened SH driven by general global cooling toward increased NH ice volume, consistent with the AMS results. Furthermore, EOA-induced increased silt production in the CAOB region may also explain the higher CAOB source contribution of the 30.9 Ma sample. On the other hand, the EOA in Central-East Asia may also have been enhanced by a strengthened SH. The dust transport pathways created by the SH after c. 31 Ma are supported by the AMS results, which also indicate more consistent NW-SE and SW-NE aligned surface winds in the magnetic zones 4a and 4b (31.0–26.9 Ma; Figures 3e and 3f). The youngest DZ sample (~29.3 Ma) has the largest northeasterly (E CAOB) source component (Figures 5 and 6c), possibly indicating an even stronger SH at that time. A stronger SH is consistent with the global cooling trend from c. 29.6 Ma onwards, although during the deposition of the composite sample, some short warmer time intervals may have occurred (Figure 6a). Despite the lack of IRD data from the ODP 913 site, the ACES IRD data suggest a slight increase in sea ice at c. 29.1 Ma (Figure 6d). Although highly speculative, assuming the ACES data represent an increased NH ice volume at ~29.1 Ma, the main difference in the contemporary environments between the 30.9 and ~29.3 Ma samples would thus be the NH polar ice extent. These samples were deposited during similar global cooling trends and, in general, showed similar benthic $\delta^{18}\text{O}$ levels ($>\sim 2.2\text{‰}$; Figure 6a). Thus, the relatively weaker SH at 30.9 Ma compared to ~29.3 Ma could be caused by the presumed lesser extent of NH polar ice. Although such an inference would be consistent with the observations from the 33.1 and 32.5 Ma provenance data discussed in the previous paragraph, more evidence on the NH polar ice extent, together with provenance data from a sample with a better age constraint than that of the composite sample, is needed to verify it. Furthermore, it is possible that the composite sample includes shorter time periods with relatively warm climate states (with $\delta^{18}\text{O}$ levels down to $\sim 1.9\text{‰}$) despite the generally high $\delta^{18}\text{O}$ levels ($>\sim 2.2\text{‰}$) during 29.5–28.8 Ma. However, to demonstrate the link between a stronger SH and a weaker westerly source contribution, we modeled the mean source contributions from four strong and weak present day EAWM years and found that a strong EAWM (strongly linked to the SH) weakens the westerly source contribution when compared to weak EAWM years (Figure S5 in Supporting Information S1). This is consistent with our provenance data, as the two youngest DZ samples have the lowest westerly (NTP) source contributions of the record (Figures 5 and 6c).

Although our data indicate a connection between NH ice volume and Ullatatal dust provenance, many uncertainties remain regarding the exact processes that form this possible link. A major uncertainty relates to the timescale. The AO and the SH are phenomena of interannual or seasonal scales, while the Ullatatal dust sequence accumulated over millions of years. However, as a Paleogene thermal contrast between the high and low latitudes

was obviously present, as expected from the lower solar radiation in the poles and inferred from bipolar glaciation, midlatitude planetary westerly winds and AO-like conditions similar to today would have likely existed. Regarding the SH, despite the Paleogene paleogeography difference, the main Eurasian continental land mass in the Siberian-Mongolian region was already present (Figure 1b), enabling the development of East Asian seasonal thermal contrasts between the land and the sea and thus, the SH. Furthermore, an increased NH ice volume as one of the controlling factors of Ulanatatal dust provenance is supported by Quaternary glacial-interglacial fluctuations in the SH strength and loess formation (Wyrwoll et al., 2016). Our results imply that even a relatively small NH ice volume consisting only of eastern Greenland ice sheets and Arctic sea ice (Spray et al., 2019; Tripathi & Darby, 2018) may be sufficient to trigger SH intensification in Asia. However, the exact mechanisms by which NH ice volume affects the SH, whether it is extensive snow cover in Eurasia (Jhun & Lee, 2004; Lü et al., 2019; Watanabe & Nitta, 1999) or some other mechanism, is beyond the scope of this work. Furthermore, the teleconnections between even the modern climate components are not well understood yet (e.g., He et al., 2017; C. Wang, Yao, et al., 2021; Wu & Wang, 2002), and further complexity is created by the lack of understanding of their relative impacts on Central-East Asian dust activity (e.g., Mao et al., 2011; Wyrwoll et al., 2016), especially on long time scales. Our provenance results provide insights for future research on these topics, and support previous claims of the prevalence of the Asian wind systems over long time scales (Licht, Dupont-Nivet, et al., 2016; Pan et al., 2023).

Tripathi and Darby (2018) argue for a relatively stable NH cryosphere until 26.5 Ma, after which the ODP 913 sediment record ends. However, it is unclear for how long Ulanatatal dust deposition continued after the preserved dust record termination at c. 27 Ma, as the Ulanatatal Formation is capped by an erosional surface and overlain by early Miocene deposits (Z. Zhang et al., 2016). There is also uncertainty over late Oligocene-early Miocene NH ice volume, although at least in the early-middle Miocene, global climate was warmer and NH ice-volume likely decreased significantly (Knies & Gaina, 2008). Many studies point to the expansion, previously interpreted as the onset, of NH glacial ice in the mid-Miocene (c. 15–13 Ma; Immonen, 2013; Knies & Gaina, 2008; Moran et al., 2006) and perhaps again in the late Miocene (c. 7 Ma; Helland & Holmes, 1997; Krissek, 1995; Larsen et al., 1994), which likely strongly influenced the onset of the Red Clay deposition in the eastern and northern CLP (e.g., Lu et al., 2010; H. Zhang et al., 2022). In the western CLP, eolian dust deposition started in the late Oligocene and continued until the Pliocene (Guo et al., 2002; Qiang et al., 2011). Indeed, our results imply that NH ice volume possibly controls northern CLP Paleogene dust deposition through intensified northwesterly winds. Similarly, Neogene northern CLP Red Clay provenance indicates that dust was mostly transported by the northwesterly winds, whereas the western CLP dust received more input via the westerlies (e.g., Shang et al., 2016). As such, even if the Arctic region was free from ice during the late Oligocene to mid-Miocene, the western CLP would have received dust via the westerlies, whereas the northern CLP dust transporting winds would likely have been too weak to allow dust deposition. However, we emphasize that this model is highly speculative as the absence of northern CLP late Oligocene-middle Miocene eolian dust records could also be explained by erosion (Meijer & van der Meulen, 2023). Indeed, Figure 7b also suggests that the Ulanatatal area could be a significant source of Baode dust today. This also raises the possibility that the Ulanatatal dust deposits themselves may have acted as sources for the Baode Red Clay in the late Miocene, as indicated by their identical DZ age distributions (Figure 7a). Loess dust is very susceptible to erosion, especially in terrestrial basins (such as Bayanhot Basin) that are not foreland basins (Meijer & van der Meulen, 2023). Furthermore, a period of uplift in the Helan Mts. occurred at c. 12–10 Ma (Liu et al., 2010) (in fact, the whole rift system surrounding the Ordos Basin was tectonically active at ~10 Ma; H. Peng et al., 2022 and references therein), which could have induced erosion and prevented the deposition in the nearby Bayanhot Basin. Tectonic instability may also explain the absence of northern CLP dust deposits during the mid-Miocene NH glacial ice expansion. If late Oligocene to mid-Miocene loess deposits in the northern CLP region existed, such a “proto-CLP” with its depocenter slightly northwest of the current CLP position could indicate the relative weakness of Paleogene-early Neogene northwesterly winds in comparison to those of the late Neogene-Quaternary, depositing the dust closer to the source regions, or simply the paleolatitudinal movement of the land and/or paleolatitudinal changes in the wind systems. A leeward eastward/southeastward migration of the “proto-CLP” to its current position is also possible if Ulanatatal dust deposits were sources for Baode Red Clay, as our results may imply. A somewhat similar recycling process of older dust deposits has been suggested by Kapp et al. (2015) and Licht, Pullen, et al. (2016) for Quaternary loess. The possibility of more wide-spread late Oligocene-mid Miocene dust deposition than that preserved and found should therefore be further investigated (Lu et al., 2010).

6. Conclusions

Here we investigate the sources of the c. 35–29 Ma Ulanatal dust record from Bayanhot Basin, 400 km NW of the CLP, by combining single-grain DZ and rutile provenance analysis and AMS measurements. The results reveal a modern-type Paleogene dust transport regime characterized by a combination of prevailing westerlies driven by planetary circulation, and northerly/northwesterly wind primarily driven by the SH/EAWM. However, we only find evidence of SH-modulated northwesterly dust transport after the EOT and argue that in the warmhouse Eocene, northwesterly wind dust transport was dominated by a long-term negative phase of AO-like conditions. As our results reveal the similarity of the Paleogene dust cycle to that of the Neogene-Quaternary, we conclude that global cooling, and possibly an Eocene-Oligocene NH ice volume increase, were the main controls of late Paleogene dust provenance under a situation analogous to Neogene and Quaternary bipolar glaciation conditions. Furthermore, we discuss the possible effects of the middle- and late Miocene NH ice volume increase on the northern CLP dust deposition, which may only be enabled if northwesterly dust transport is substantial. While the late Miocene dust deposits are relatively wide-spread, middle Miocene dust deposition may have been prevented by tectonic activity in the region. Our results also have wider impacts on understanding the mechanisms of the CLP formation, evolution and modification on long time scales and under warmer climates. Modern-type atmospheric components may be used to explain past wind regimes, but more research is needed to reveal the specific long-term links between NH ice volume and the Central-East Asian dust cycle.

Data Availability Statement

The anisotropy of magnetic susceptibility data, detrital zircon U-Pb data, and detrital rutile trace element data used in the study are openly available at Fairdata IDA via <https://doi.org/10.23729/7f457d0b-be68-4c89-9f81-0017154ce1b8> (Bohm et al., 2023) with Creative Commons Attribution 4.0 International (CC BY 4.0) license.

Acknowledgments

We thank the four anonymous reviewers for their constructive comments that helped to improve the manuscript. This research was supported by Magnus Ehrnrooth foundation grant to KB, Research Council of Finland grant (316799) to AK, a Swedish Research Council (2017–03888) grant and STINT-NSFC mobility grants (CH2020-8688 and 42111530183) to TS, and Research Council of Finland grants to JS (Grant 288277) and HT (Grant 337552). The simulations were performed on resources provided by Sigma2—the National Infrastructure for High Performance Computing and Data Storage in Norway. ERA5 data used in this study were downloaded using the Copernicus Climate Change Service (C3S) Climate Data Store. Neither the European Commission nor ECMWF is responsible for any use that may be made of the information it contains. We are grateful to the Ivar Giæver Geomagnetic Laboratory (IGGL) for the use of their facilities. The IGGL is funded by the Research Council of Norway (project number 226214) and the Centre for Earth Evolution and Dynamics, University of Oslo. The Ulanatal project was supported by the Strategic Research Program of Chinese Academy of Sciences (XDB26000000). We thank IVPP colleagues who participated in the Ulanatal field seasons.

References

- Abell, J. T., Winckler, G., Pullen, A., Kinsley, C. W., Kapp, P. A., Middleton, J. L., et al. (2023). Evaluating the drivers of quaternary dust fluxes to the western North Pacific: East Asian dustiness and Northern Hemisphere dustiness. *Paleoceanography and Paleoclimatology*, 38(9), e2022PA004571. <https://doi.org/10.1029/2022PA004571>
- Abels, H. A., Dupont-Nivet, G., Xiao, G., Bosboom, R., & Krijgsman, W. (2011). Step-wise change of Asian interior climate preceding the Eocene–Oligocene transition (EOT). *Palaeogeography, Palaeoclimatology, Palaeoecology*, 299(3), 399–412. <https://doi.org/10.1016/j.palaeo.2010.11.028>
- Adebisi, A. A., & Kok, J. F. (2020). Climate models miss most of the coarse dust in the atmosphere. *Science Advances*, 6(15), eaaz9507. <https://doi.org/10.1126/sciadv.aaz9507>
- Aminov, J., Dupont-Nivet, G., Ruiz, D., & Gailleton, B. (2023). Paleogeographic reconstructions using QGIS: Introducing Terra Antiqua plugin and its application to 30 and 50 Ma maps. *Earth-Science Reviews*, 240, 104401. <https://doi.org/10.1016/j.earscirev.2023.104401>
- An, Z. (2000). The history and variability of the East Asian paleomonsoon climate. *Quaternary Science Reviews*, 19(1), 171–187. [https://doi.org/10.1016/S0277-3791\(99\)00060-8](https://doi.org/10.1016/S0277-3791(99)00060-8)
- Ao, H., Dupont-Nivet, G., Rohling, E. J., Zhang, P., Ladant, J.-B., Roberts, A. P., et al. (2020). Orbital climate variability on the northeastern Tibetan Plateau across the Eocene–Oligocene transition. *Nature Communications*, 11(1), 5249. <https://doi.org/10.1038/s41467-020-18824-8>
- Axelsson, E., Pape, J., Berndt, J., Corfu, F., Mezger, K., & Raith, M. M. (2018). Rutile R632—A new natural reference material for U-Pb and Zr determination. *Geostandards and Geoanalytical Research*, 42(3), 319–338. <https://doi.org/10.1111/ggr.12213>
- Barry, T. L., Saunders, A. D., Kempton, P. D., Windley, B. F., Pringle, M. S., Dorjnamjaa, D., & Saandar, S. (2003). Petrogenesis of Cenozoic Basalts from Mongolia: Evidence for the role of Asthenospheric versus metasomatized lithospheric Mantle sources. *Journal of Petrology*, 44(1), 55–91. <https://doi.org/10.1093/petrology/44.1.55>
- Bird, A., Stevens, T., Rittner, M., Vermeesch, P., Carter, A., Andò, S., et al. (2015). Quaternary dust source variation across the Chinese Loess Plateau. *Paleoceanography, Palaeoclimatology, Palaeoecology*, 435, 254–264. <https://doi.org/10.1016/j.palaeo.2015.06.024>
- Bohm, K., Kaakinen, A., Stevens, T., Lahaye, Y., O'Brien, H., Tang, H., et al. (2023a). Neogene global climate change and East Asian dust sources: Combined rutile geochemistry and zircon U-Pb analysis from the northern Chinese Loess Plateau. *Global and Planetary Change*, 221, 104049. <https://doi.org/10.1016/j.gloplacha.2023.104049>
- Bohm, K., Kaakinen, A., Stevens, T., Lahaye, Y., O'Brien, H., Tang, H., et al. (2023b). Detrital zircon U-Pb age and detrital rutile trace element data from the late Neogene Baode Red Clay sequence, Chinese Loess Plateau, and detrital rutile geochemistry from 14 potential source areas [Dataset]. PANGAEA. <https://doi.org/10.1594/PANGAEA.951048>
- Bohm, K., Stevens, T., Kaakinen, A., Lahaye, Y., O'Brien, H., & Zhang, Z. (2022). The provenance of late Cenozoic East Asian Red Clay: Tectonic-metamorphic history of potential source regions and a novel combined zircon-rutile approach. *Earth-Science Reviews*, 225, 103909. <https://doi.org/10.1016/j.earscirev.2021.103909>
- Bohm, K., Wasiljeff, J., Kaakinen, A., Stevens, T., Salminen, J., Lahaye, Y., et al. (2023). Single-grain detrital zircon U-Pb and detrital rutile geochemistry data, and anisotropy of magnetic susceptibility data from a Paleogene aeolian dust sequence in Ulanatal, Inner Mongolia, China (Version 1) [Dataset]. University of Helsinki. <https://doi.org/10.23729/7f457d0b-be68-4c89-9f81-0017154ce1b8>
- Börker, J., Hartmann, J., Amann, T., & Romero-Mujalli, G. (2018). Global Unconsolidated Sediments Map Database v1.0 (shapefile and gridded to 0.5° spatial resolution) [Dataset]. PANGAEA. <https://doi.org/10.1594/PANGAEA.884822>
- Borradaile, G. (1987). Anisotropy of magnetic susceptibility: Rock composition versus strain. *Tectonophysics*, 138(2), 327–329. [https://doi.org/10.1016/0040-1951\(87\)90051-5](https://doi.org/10.1016/0040-1951(87)90051-5)

- Bosboom, R. E., Abels, H. A., Hoorn, C., van den Berg, B. C. J., Guo, Z., & Dupont-Nivet, G. (2014). Aridification in continental Asia after the middle Eocene climatic Optimum (MECO). *Earth and Planetary Science Letters*, 389, 34–42. <https://doi.org/10.1016/j.epsl.2013.12.014>
- Bradák, B., Seto, Y., Chadima, M., Kovács, J., Tanos, P., Újvári, G., & Hyodo, M. (2020). Magnetic fabric of loess and its significance in Pleistocene environment reconstructions. *Earth-Science Reviews*, 210, 103385. <https://doi.org/10.1016/j.earscirev.2020.103385>
- Bradák, B., Újvári, G., Seto, Y., Hyodo, M., & Végh, T. (2018). A conceptual magnetic fabric development model for the Paks loess in Hungary. *Aeolian Research*, 30, 20–31. <https://doi.org/10.1016/j.aeolia.2017.11.002>
- Bush, M. A., Saylor, J. E., Horton, B. K., & Nie, J. (2016). Growth of the Qaidam Basin during Cenozoic exhumation in the northern Tibetan Plateau: Inferences from depositional patterns and multiproxy detrital provenance signatures. *Lithosphere*, 8(1), 58–82. <https://doi.org/10.1130/L449.1>
- Caves, J. K., Winnick, M. J., Graham, S. A., Sjöström, D. J., Mulch, A., & Chamberlain, C. P. (2015). Role of the westerlies in central Asia climate over the Cenozoic. *Earth and Planetary Science Letters*, 428, 33–43. <https://doi.org/10.1016/j.epsl.2015.07.023>
- Che, X., & Li, G. (2013). Binary sources of loess on the Chinese Loess Plateau revealed by U–Pb ages of zircon. *Quaternary Research*, 80(3), 545–551. <https://doi.org/10.1016/j.yqres.2013.05.007>
- Chen, S., Huang, J., Qian, Y., Zhao, C., Kang, L., Yang, B., et al. (2017). An overview of mineral dust modeling over East Asia. *Journal of Meteorological Research*, 31(4), 633–653. <https://doi.org/10.1007/s13351-017-6142-2>
- Coxall, H. K., Wilson, P. A., Pälike, H., Lear, C. H., & Backman, J. (2005). Rapid stepwise onset of Antarctic glaciation and deeper calcite compensation in the Pacific Ocean. *Nature*, 433(7021), 53–57. <https://doi.org/10.1038/nature03135>
- Ding, L. I. N., Kapp, P., Zhong, D., & Deng, W. (2003). Cenozoic volcanism in Tibet: Evidence for a transition from oceanic to continental subduction. *Journal of Petrology*, 44(10), 1833–1865. <https://doi.org/10.1093/petrology/egg061>
- Dupont-Nivet, G., Krijgsman, W., Langereis, C. G., Abels, H. A., Dai, S., & Fang, X. (2007). Tibetan plateau aridification linked to global cooling at the Eocene–Oligocene transition. *Nature*, 445(7128), 635–638. <https://doi.org/10.1038/nature05516>
- Edgar, K. M., Wilson, P. A., Sexton, P. F., & Suganuma, Y. (2007). No extreme bipolar glaciation during the main Eocene calcite compensation shift. *Nature*, 448(7156), 908–911. <https://doi.org/10.1038/nature06053>
- Eldrett, J. S., Harding, I. C., Wilson, P. A., Butler, E., & Roberts, A. P. (2007). Continental ice in Greenland during the Eocene and Oligocene. *Nature*, 446(7132), 176–179. <https://doi.org/10.1038/nature05591>
- Fang, X., Dupont-Nivet, G., Wang, C., Song, C., Meng, Q., Zhang, W., et al. (2020). Revised chronology of central Tibet uplift (Lunpola basin). *Science Advances*, 6(50), eaba7298. <https://doi.org/10.1126/sciadv.aba7298>
- Farnsworth, A., Lunt, D. J., Robinson, S. A., Valdes, P. J., Roberts, W. H. G., Clift, P. D., et al. (2019). Past East Asian monsoon evolution controlled by paleogeography, not CO₂. *Science Advances*, 5(10), eaax1697. <https://doi.org/10.1126/sciadv.aax1697>
- Fenn, K., Stevens, T., Bird, A., Limonta, M., Rittner, M., Vermeesch, P., et al. (2018). Insights into the provenance of the Chinese Loess Plateau from joint zircon U–Pb and garnet geochemical analysis of last glacial loess. *Quaternary Research*, 89(3), 645–659. <https://doi.org/10.1017/qua.2017.86>
- Gradstein, F. M., Ogg, J. G., & Smith, A. G. (2005). *A geologic time scale 2004*. Cambridge University Press.
- Groot Zwaafink, C. D., Arnalds, Ó., Dagsson-Waldhauserova, P., Eckhardt, S., Prospero, J. M., & Stohl, A. (2017). Temporal and spatial variability of Icelandic dust emissions and atmospheric transport. *Atmospheric Chemistry and Physics*, 17(17), 10865–10878. <https://doi.org/10.5194/acp-17-10865-2017>
- Guo, Z. T., Ruddiman, W. F., Hao, Q. Z., Wu, H. B., Qiao, Y. S., Zhu, R. X., et al. (2002). Onset of Asian desertification by 22 Myr ago inferred from loess deposits in China. *Nature*, 416(6877), 159–163. <https://doi.org/10.1038/416159a>
- Harzhauser, M., Daxner-Höck, G., López-Guerrero, P., Maridet, O., Oliver, A., Piller, W. E., et al. (2016). Stepwise onset of the Icehouse world and its impact on Oligo-Miocene central Asian mammals. *Scientific Reports*, 6(1), 36169. <https://doi.org/10.1038/srep36169>
- He, S., Gao, Y., Li, F., Wang, H., & He, Y. (2017). Impact of Arctic Oscillation on the East Asian climate: A review. *Earth-Science Reviews*, 164, 48–62. <https://doi.org/10.1016/j.earscirev.2016.10.014>
- Helland, P. E., & Holmes, M. A. (1997). Surface textural analysis of quartz sand grains from ODP Site 918 off the southeast coast of Greenland suggests glaciation of southern Greenland at 11 Ma. *Palaeogeography, Palaeoclimatology, Palaeoecology*, 135(1), 109–121. [https://doi.org/10.1016/S0031-0182\(97\)00025-4](https://doi.org/10.1016/S0031-0182(97)00025-4)
- Hersbach, H., Bell, B., Berrisford, P., Biavati, G., Horányi, A., Muñoz Sabater, J., et al. (2023). ERA5 hourly data on single levels from 1940 to present. In *Copernicus climate change Service (C3S) climate data store (CDS)*.
- Horstwood, M. S. A., Košler, J., Gehrels, G., Jackson, S. E., McLean, N. M., Paton, C., et al. (2016). Community-derived standards for LA-ICP-MS U–(Th)–Pb geochronology—Uncertainty propagation, age interpretation and data reporting. *Geostandards and Geoanalytical Research*, 40(3), 311–332. <https://doi.org/10.1111/j.1751-908X.2016.00379.x>
- Huhma, H., Mänttari, I., Peltonen, P., Kontinen, A., Halkoaho, T., Hanski, E., et al. (2012). The age of the Archaean greenstone belts in Finland. In *Geological Survey of Finland, special paper* (Vol. 54, pp. 74–175).
- Hus, J. J. (2003). The magnetic fabric of some loess/palaeosol deposits. *Physics and Chemistry of the Earth, Parts A/B/C*, 28(16), 689–699. [https://doi.org/10.1016/S1474-7065\(03\)00128-1](https://doi.org/10.1016/S1474-7065(03)00128-1)
- Immonen, N. (2013). Surface microtextures of ice-rafted quartz grains revealing glacial ice in the Cenozoic Arctic. *Palaeogeography, Palaeoclimatology, Palaeoecology*, 374, 293–302. <https://doi.org/10.1016/j.palaeo.2013.02.003>
- Jackson, S. E., Pearson, N. J., Griffin, W. L., & Belousova, E. A. (2004). The application of laser ablation-inductively coupled plasma-mass spectrometry to in situ U–Pb zircon geochronology. *Chemical Geology*, 211(1), 47–69. <https://doi.org/10.1016/j.chemgeo.2004.06.017>
- Jelinek, V. (1981). Characterization of the magnetic fabric of rocks. *Tectonophysics*, 79(3), T63–T67. [https://doi.org/10.1016/0040-1951\(81\)90110-4](https://doi.org/10.1016/0040-1951(81)90110-4)
- Jhun, J.-G., & Lee, E.-J. (2004). A new East Asian winter monsoon index and associated characteristics of the winter monsoon. *Journal of Climate*, 17(4), 711–726. [https://doi.org/10.1175/1520-0442\(2004\)017<0711:ANEAWM>2.0.CO;2](https://doi.org/10.1175/1520-0442(2004)017<0711:ANEAWM>2.0.CO;2)
- Jochum, K. P., Willbold, M., Raczek, I., Stoll, B., & Herwig, K. (2005). Chemical characterisation of the USGS reference glasses GSA-1G, GSC-1G, GSD-1G, GSE-1G, BCR-2G, BHVO-2G and BIR-1G using EPMA, ID-TIMS, ID-ICP-MS and LA-ICP-MS. *Geostandards and Geoanalytical Research*, 29(3), 285–302. <https://doi.org/10.1111/j.1751-908X.2005.tb00901.x>
- Kapp, P., & DeCelles, P. G. (2019). Mesozoic–Cenozoic geological evolution of the Himalayan–Tibetan orogen and working tectonic hypotheses. *American Journal of Science*, 319(3), 159–254. <https://doi.org/10.2475/03.2019.01>
- Kapp, P., Pullen, A., Pelletier, J. D., Russell, J., Goodman, P., & Cai, F. (2015). From dust to dust: Quaternary wind erosion of the Mu Us desert and Loess Plateau, China. *Geology*, 43(9), 835–838. <https://doi.org/10.1130/G36724.1>
- Knies, J., & Gaina, C. (2008). Middle Miocene ice sheet expansion in the Arctic: Views from the Barents sea. *Geochemistry, Geophysics, Geosystems*, 9(2), Q02015. <https://doi.org/10.1029/2007GC001824>

- Költringer, C., Bradák, B., Stevens, T., Almqvist, B., Banak, A., Lindner, M., et al. (2021). Palaeoenvironmental implications from Lower Volga loess—Joint magnetic fabric and multi-proxy analyses. *Quaternary Science Reviews*, 267, 107057. <https://doi.org/10.1016/j.quascirev.2021.107057>
- Kong, P., Jia, J., & Zheng, Y. (2014). Time constraints for the Yellow River traversing the Sanmen Gorge. *Geochemistry, Geophysics, Geosystems*, 15(2), 395–407. <https://doi.org/10.1002/2013gc004912>
- Krissek, L. A. (1995). Late Cenozoic ice-rafting records from Leg 145 sites in the North Pacific; late Miocene onset, late Pliocene intensification, and Pliocene-Pleistocene events. In *Proceedings of the ocean drilling Program; scientific results, North Pacific transect; covering Leg 145 of the cruises of the drilling vessel JOIDES Resolution, Yokohama, Japan, to Victoria, Canada, sites 881–887, 20 July–20 September 1992* (Vol. 145, p. 179). <https://doi.org/10.2973/odp.proc.sr.145.118.1995>
- Kurosaki, Y., & Mikami, M. (2003). Recent frequent dust events and their relation to surface wind in East Asia. *Geophysical Research Letters*, 30(14), 1726–1736. <https://doi.org/10.1029/2003GL017261>
- Lagroix, F., & Banerjee, S. K. (2002). Paleowind directions from the magnetic fabric of loess profiles in central Alaska. *Earth and Planetary Science Letters*, 195(1), 99–112. [https://doi.org/10.1016/S0012-821X\(01\)00564-7](https://doi.org/10.1016/S0012-821X(01)00564-7)
- Lagroix, F., & Banerjee, S. K. (2004). The regional and temporal significance of primary aeolian magnetic fabrics preserved in Alaskan loess. *Earth and Planetary Science Letters*, 225(3), 379–395. <https://doi.org/10.1016/j.epsl.2004.07.003>
- Lagroix, F., & Borradaile, G. J. (2000). Magnetic fabric interpretation complicated by inclusions in mafic silicates. *Tectonophysics*, 325(3), 207–225. [https://doi.org/10.1016/S0040-1951\(00\)00125-6](https://doi.org/10.1016/S0040-1951(00)00125-6)
- Larsen, H. C., Saunders, A. D., Clift, P. D., Beget, J., Wei, W., & Spezzaferri, S. (1994). Seven million years of glaciation in Greenland. *Science*, 264(5161), 952–955. <https://doi.org/10.1126/science.264.5161.952>
- Li, J. X., Yue, L. P., Roberts, A. P., Hirt, A. M., Pan, F., Guo, L., et al. (2018). Global cooling and enhanced Eocene Asian mid-latitude interior aridity. *Nature Communications*, 9(1), 3026. <https://doi.org/10.1038/s41467-018-05415-x>
- Li, Q., Li, L., Zhang, Y., & Guo, Z. (2020). Oligocene incursion of the Paratethys seawater to the Junggar basin, NW China: Insight from multiple isotopic analysis of carbonate. *Scientific Reports*, 10(1), 6601. <https://doi.org/10.1038/s41598-020-63609-0>
- Li, X., Zhang, R., Zhang, Z., & Yan, Q. (2018a). Do climate simulations support the existence of East Asian monsoon climate in the Late Eocene? *Palaeogeography, Palaeoclimatology, Palaeoecology*, 509, 47–57. <https://doi.org/10.1016/j.palaeo.2017.12.037>
- Li, X., Zhang, R., Zhang, Z., & Yan, Q. (2018b). What enhanced the aridity in Eocene Asian inland: Global cooling or early Tibetan Plateau uplift? *Palaeogeography, Palaeoclimatology, Palaeoecology*, 510, 6–14. <https://doi.org/10.1016/j.palaeo.2017.10.029>
- Licht, A., Dupont-Nivet, G., Pullen, A., Kapp, P., Abels, H. A., Lai, Z., et al. (2016). Resilience of the Asian atmospheric circulation shown by Paleogene dust provenance. *Nature Communications*, 7(1), 12390. <https://doi.org/10.1038/ncomms12390>
- Licht, A., Pullen, A., Kapp, P., Abell, J., & Giesler, N. (2016). Eolian cannibalism: Reworked loess and fluvial sediment as the main sources of the Chinese Loess Plateau. *GSA Bulletin*, 128(5–6), 944–956. <https://doi.org/10.1130/B31375.1>
- Licht, A., van Cappelle, M., Abels, H. A., Ladant, J. B., Trabucho-Alexandre, J., France-Lanord, C., et al. (2014). Asian monsoons in a late Eocene greenhouse world. *Nature*, 513(7519), 501–506. <https://doi.org/10.1038/nature13704>
- Liu, J., Zhang, P., Zheng, D., Wan, J., Wang, W., Du, P., & Lei, Q. (2010). Pattern and timing of late Cenozoic rapid exhumation and uplift of the Helan Mountain, China. *Science China Earth Sciences*, 53(3), 345–355. <https://doi.org/10.1007/s11430-010-0016-0>
- Lu, H., Wang, X., & Li, L. (2010). Aeolian sediment evidence that global cooling has driven late Cenozoic stepwise aridification in central Asia. *Geological Society, London, Special Publications*, 342(1), 29–44. <https://doi.org/10.1144/SP342.4>
- Lu, H., Wang, X., Wang, X., Chang, X., Zhang, H., Xu, Z., et al. (2019). Formation and evolution of Gobi desert in central and eastern Asia. *Earth-Science Reviews*, 194, 251–263. <https://doi.org/10.1016/j.earscirev.2019.04.014>
- Lü, Z., He, S., Li, F., & Wang, H. (2019). Impacts of the Autumn Arctic sea ice on the intraseasonal reversal of the winter Siberian high. *Advances in Atmospheric Sciences*, 36(2), 173–188. <https://doi.org/10.1007/s00376-017-8089-8>
- Luvizotto, G. L., Zack, T., Meyer, H. P., Ludwig, T., Triebold, S., Kronz, A., et al. (2009). Rutile crystals as potential trace element and isotope mineral standards for microanalysis. *Chemical Geology*, 261(3), 346–369. <https://doi.org/10.1016/j.chemgeo.2008.04.012>
- Mao, R., Ho, C.-H., Shao, Y., Gong, D.-Y., & Kim, J. (2011). Influence of Arctic Oscillation on dust activity over northeast Asia. *Atmospheric Environment*, 45(2), 326–337. <https://doi.org/10.1016/j.atmosenv.2010.10.020>
- Martin, J. H. (1990). Glacial-interglacial CO₂ change: The Iron hypothesis. *Paleoceanography*, 5(1), 1–13. <https://doi.org/10.1029/PA005i001p00001>
- Meijer, N., Dupont-Nivet, G., Abels, H. A., Kaya, M. Y., Licht, A., Xiao, M., et al. (2019). Central Asian moisture modulated by proto-Paratethys Sea incursions since the early Eocene. *Earth and Planetary Science Letters*, 510, 73–84. <https://doi.org/10.1016/j.epsl.2018.12.031>
- Meijer, N., & van der Meulen, B. (2023). Loss of loess in the geological record due to poor preservation. *Terra Nova*, 35(3), 185–192. <https://doi.org/10.1111/ter.12642>
- Moran, K., Backman, J., Brinkhuis, H., Clemens, S. C., Cronin, T., Dickens, G. R., et al. (2006). The cenozoic palaeoenvironment of the Arctic Ocean. *Nature*, 441(7093), 601–605. <https://doi.org/10.1038/nature04800>
- Nawrocki, J., Polechońska, O., Bogucki, A., & Łanczont, M. (2006). Palaeowind directions recorded in the youngest loess in Poland and western Ukraine as derived from anisotropy of magnetic susceptibility measurements. *Boreas*, 35(2), 266–271. <https://doi.org/10.1111/j.1502-3885.2006.tb01156.x>
- Nie, J., Pullen, A., Garzzone, C. N., Peng, W., & Wang, Z. (2018). Pre-quaternary decoupling between Asian aridification and high dust accumulation rates. *Science Advances*, 4(2), eaao6977. <https://doi.org/10.1126/sciadv.aao6977>
- Nie, J., Stevens, T., Rittner, M., Stockli, D., Garzanti, E., Limonta, M., et al. (2015). Loess Plateau storage of northeastern Tibetan plateau-derived Yellow River sediment. *Nature Communications*, 6(1), 8511. <https://doi.org/10.1038/ncomms9511>
- Pan, F., Li, J., Nie, J., Xu, Y., & Yue, L. (2023). Provenance of eolian deposits in the Xorkol Basin: Implications for Eocene dust-transport pattern in western China. *GSA Bulletin*. <https://doi.org/10.1130/B36274.1>
- Peng, H., Wang, J., Liu, C., Huang, L., & Zattin, M. (2022). Mesozoic exhumation and ca. 10 Ma reactivation of the southern Yin Shan, North China, revealed by low-temperature thermochronology. *Tectonophysics*, 823, 229189. <https://doi.org/10.1016/j.tecto.2021.229189>
- Peng, W., Zhang, H., Pullen, A., Li, M., Pan, B., Xiao, W., & Nie, J. (2023). Stepwise increased spatial provenance contrast on the Chinese Loess Plateau over late Miocene-Pleistocene. *Communications Earth & Environment*, 4(1), 60. <https://doi.org/10.1038/s43247-023-00721-9>
- Pisso, I., Sollum, E., Grythe, H., Kristiansen, N. I., Cassiani, M., Eckhardt, S., et al. (2019). The Lagrangian particle dispersion model FLEXPART version 10.4. *Geoscientific Model Development*, 12(12), 4955–4997. <https://doi.org/10.5194/gmd-12-4955-2019>
- Pullen, A., Kapp, P., McCallister, A. T., Chang, H., Gehrels, G. E., Garzzone, C. N., et al. (2011). Qaidam Basin and northern Tibetan Plateau as dust sources for the Chinese Loess Plateau and paleoclimatic implications. *Geology*, 39(11), 1031–1034. <https://doi.org/10.1130/g32296.1>
- Pye, K. (1987). *Aeolian dust and dust deposits*. Academic Press.

- Qiang, X., An, Z., Song, Y., Chang, H., Sun, Y., Liu, W., et al. (2011). New eolian red clay sequence on the western Chinese Loess Plateau linked to onset of Asian desertification about 25 Ma ago. *Science China Earth Sciences*, 54(1), 136–144. <https://doi.org/10.1007/s11430-010-4126-5>
- Rea, D. K., Snoeckx, H., & Joseph, L. H. (1998). Late Cenozoic Eolian deposition in the North Pacific: Asian drying, Tibetan uplift, and cooling of the northern hemisphere. *Paleoceanography*, 13(3), 215–224. <https://doi.org/10.1029/98pa00123>
- Rochette, P., Jackson, M., & Aubourg, C. (1992). Rock magnetism and the interpretation of anisotropy of magnetic susceptibility. *Reviews of Geophysics*, 30(3), 209–226. <https://doi.org/10.1029/92RG00733>
- Roe, G. (2009). On the interpretation of Chinese loess as a paleoclimate indicator. *Quaternary Research*, 71(2), 150–161. <https://doi.org/10.1016/j.yqres.2008.09.004>
- Schudel, G., Lai, V., Gordon, K., & Weis, D. (2015). Trace element characterization of USGS reference materials by HR-ICP-MS and Q-ICP-MS. *Chemical Geology*, 410, 223–236. <https://doi.org/10.1016/j.chemgeo.2015.06.006>
- Shang, Y., Beets, C. J., Tang, H., Prins, M. A., Lahaye, Y., van Elsas, R., et al. (2016). Variations in the provenance of the late Neogene Red Clay deposits in northern China. *Earth and Planetary Science Letters*, 439, 88–100. <https://doi.org/10.1016/j.epsl.2016.01.031>
- Shao, Y., & Wang, J. (2003). A climatology of Northeast Asian dust events. *Meteorologische Zeitschrift*, 12(4), 187–196. <https://doi.org/10.1127/0941-2948/2003/0012-0187>
- Sláma, J., Košler, J., Condon, D. J., Crowley, J. L., Gerdes, A., Hanchar, J. M., et al. (2008). Plešovice zircon—A new natural reference material for U–Pb and Hf isotopic microanalysis. *Chemical Geology*, 249(1), 1–35. <https://doi.org/10.1016/j.chemgeo.2007.11.005>
- Spicer, R. A., Yang, J., Herman, A., Kodrul, T., Aleksandrova, G., Maslova, N., et al. (2017). Paleogene monsoons across India and South China: Drivers of biotic change. *Gondwana Research*, 49, 350–363. <https://doi.org/10.1016/j.gr.2017.06.006>
- Spicer, R. A., Su, T., Valdes, P. J., Farnsworth, A., Wu, F.-X., Shi, G., et al. (2020). Why ‘the uplift of the Tibetan Plateau’ is a myth. *National Science Review*, 8(1), 19. <https://doi.org/10.1093/nsr/nwaa091>
- Spray, J. F., Bohaty, S. M., Davies, A., Bailey, I., Romans, B. W., Cooper, M. J., et al. (2019). North Atlantic evidence for a unipolar icehouse climate state at the Eocene-Oligocene transition. *Paleoceanography and Paleoclimatology*, 34(7), 1124–1138. <https://doi.org/10.1029/2019PA003563>
- Stacey, J. S., & Kramers, J. D. (1975). Approximation of terrestrial lead isotope evolution by a two-stage model. *Earth and Planetary Science Letters*, 26(2), 207–221. [https://doi.org/10.1016/0012-821X\(75\)90088-6](https://doi.org/10.1016/0012-821X(75)90088-6)
- Stevens, T., Carter, A., Palk, C., Lu, H., & Clift, P. D. (2010). Assessing the provenance of loess and desert sediments in northern China using U–Pb dating and morphology of detrital zircons. *GSA Bulletin*, 122(7–8), 1331–1344. <https://doi.org/10.1130/B30102.1>
- Stevens, T., Carter, A., Watson, T. P., Vermeesch, P., Andò, S., Bird, A. F., et al. (2013). Genetic linkage between the Yellow River, the Mu Us desert and the Chinese Loess Plateau. *Quaternary Science Reviews*, 78, 355–368. <https://doi.org/10.1016/j.quascirev.2012.11.032>
- Su, T., Farnsworth, A., Spicer, R. A., Huang, J., Wu, F.-X., Liu, J., et al. (2019). No high Tibetan plateau until the Neogene. *Science Advances*, 5(3), eaav2189. <https://doi.org/10.1126/sciadv.aav2189>
- Sun, J., Ding, Z., Xiao, W., & Windley, B. F. (2022). Coupling between uplift of the central Asian Orogenic Belt-NE Tibetan plateau and accumulation of aeolian red clay in the inner Asia began at ~7 Ma. *Earth-Science Reviews*, 226, 103919. <https://doi.org/10.1016/j.earscirev.2022.103919>
- Sun, Y., Yan, Y., Nie, J., Li, G., Shi, Z., Qiang, X., et al. (2020). Source-to-sink fluctuations of Asian aeolian deposits since the late Oligocene. *Earth-Science Reviews*, 200, 102963. <https://doi.org/10.1016/j.earscirev.2019.102963>
- Sundell, K. E., & Saylor, J. E. (2017). Unmixing detrital geochronology age distributions. *Geochemistry, Geophysics, Geosystems*, 18(8), 2872–2886. <https://doi.org/10.1002/2016GC006774>
- Tang, H., Haugvaldstad, O. W., Stordal, F., Bi, J., Groot Zwaafink, C. D., Grythe, H., et al. (2023). Modelling the 2021 East Asia super dust storm using FLEXPART and FLEXDUST and its comparison with reanalyses and observations. *Frontiers in Environmental Science*, 10, 1013875. <https://doi.org/10.3389/fenvs.2022.1013875>
- Tardif, D., Fluteau, F., Donnadiou, Y., Le Hir, G., Ladant, J. B., Sepulchre, P., et al. (2020). The origin of Asian monsoons: A modelling perspective. *Climate of the Past*, 16(3), 847–865. <https://doi.org/10.5194/cp-16-847-2020>
- Tarling, D. H., & Hrouda, F. (1993). *The magnetic anisotropy of rocks*. Chapman & Hall.
- Taylor, S. N., & Lagroix, F. (2015). Magnetic anisotropy reveals the depositional and postdepositional history of a loess-paleosol sequence at Nussloch (Germany). *Journal of Geophysical Research: Solid Earth*, 120(5), 2859–2876. <https://doi.org/10.1002/2014JB011803>
- Tegen, I., Lacis, A. A., & Fung, I. (1996). The influence on climate forcing of mineral aerosols from disturbed soils. *Nature*, 380(6573), 419–422. <https://doi.org/10.1038/380419a0>
- Tomkins, H. S., Powell, R., & Ellis, D. J. (2007). The pressure dependence of the zirconium-in-rutile thermometer. *Journal of Metamorphic Geology*, 25(6), 703–713. <https://doi.org/10.1111/j.1525-1314.2007.00724.x>
- Triebold, S., Luvizotto, G. L., Tolosana-Delgado, R., Zack, T., & von Eynatten, H. (2011). Discrimination of TiO₂ polymorphs in sedimentary and metamorphic rocks. *Contributions to Mineralogy and Petrology*, 161(4), 581–596. <https://doi.org/10.1007/s00410-010-0551-x>
- Triebold, S., von Eynatten, H., & Zack, T. (2012). A recipe for the use of rutile in sedimentary provenance analysis. *Sedimentary Geology*, 282, 268–275. <https://doi.org/10.1016/j.sedgeo.2012.09.008>
- Tripathi, A., Backman, J., Elderfield, H., & Ferretti, P. (2005). Eocene bipolar glaciation associated with global carbon cycle changes. *Nature*, 436(7049), 341–346. <https://doi.org/10.1038/nature03874>
- Tripathi, A., & Darby, D. (2018). Evidence for ephemeral middle Eocene to early Oligocene Greenland glacial ice and pan-Arctic sea ice. *Nature Communications*, 9(1), 1038. <https://doi.org/10.1038/s41467-018-03180-5>
- Van Achterberg, E., Ryan, C., Jackson, S., & Griffin, W. (2001). Data reduction software for LA-ICP-MS. *Laser Ablation ICP-MS in the Earth Science*, 29, 239–243.
- Vermeesch, P., Resentini, A., & Garzanti, E. (2016). An R package for statistical provenance analysis. *Sedimentary Geology*, 336, 14–25. <https://doi.org/10.1016/j.sedgeo.2016.01.009>
- Wang, C., Yao, Y., Wang, H., Sun, X., & Zheng, J. (2021). The 2020 summer floods and 2020/21 winter extreme cold surges in China and the 2020 Typhoon season in the western North Pacific. *Advances in Atmospheric Sciences*, 38(6), 896–904. <https://doi.org/10.1007/s00376-021-1094-y>
- Wang, S., Yu, Y., Zhang, X.-X., Lu, H., Zhang, X.-Y., & Xu, Z. (2021). Weakened dust activity over China and Mongolia from 2001 to 2020 associated with climate change and land-use management. *Environmental Research Letters*, 16(12), 124056. <https://doi.org/10.1088/1748-9326/ac3b79>
- Wang, Y., Lu, H., Lyu, H., Cai, D., Qiang, X., Li, Y., et al. (2023). East Asian hydroclimate responses to the Eocene-Oligocene transition in the Weihe basin, central China. *Palaeogeography, Palaeoclimatology, Palaeoecology*, 615, 111436. <https://doi.org/10.1016/j.palaeo.2023.111436>

- Wasiljeff, J., Kaakinen, A., Salminen, J. M., & Zhang, Z. (2020). Magnetostratigraphic constraints on the fossiliferous Ulanatal sequence in Inner Mongolia, China: Implications for Asian aridification and faunal turnover before the Eocene-Oligocene boundary. *Earth and Planetary Science Letters*, 535, 116125. <https://doi.org/10.1016/j.epsl.2020.116125>
- Wasiljeff, J., Salminen, J. M., Stenman, J., Zhang, Z., & Kaakinen, A. (2022). Oligocene moisture variations as evidenced by an aeolian dust sequence in Inner Mongolia, China. *Scientific Reports*, 12(1), 5597. <https://doi.org/10.1038/s41598-022-09362-y>
- Wasiljeff, J., & Zhang, Z. (2022). Stratigraphical significance of Ulanatal sequence (Nei Mongol, China) in refining the latest Eocene and Oligocene terrestrial regional stages. In *Vertebrata Palasiatica* (Vol. 55, pp. 1–12).
- Watanabe, M., & Nitta, T. (1999). Decadal changes in the atmospheric circulation and associated surface climate variations in the northern hemisphere winter. *Journal of Climate*, 12(2), 494–510. [https://doi.org/10.1175/1520-0442\(1999\)012<0494:DCITAC>2.0.CO;2](https://doi.org/10.1175/1520-0442(1999)012<0494:DCITAC>2.0.CO;2)
- Wen, L., Lu, H., & Qiang, X. (2005). Changes in grain-size and sedimentation rate of the Neogene Red Clay deposits along the Chinese Loess Plateau and implications for the palaeowind system. *Science in China Series D: Earth Sciences*, 48(9), 1452–1462. <https://doi.org/10.1360/01yd0558>
- Westerhold, T., Marwan, N., Drury, A. J., Liebrand, D., Agnini, C., Anagnostou, E., et al. (2020). An astronomically dated record of Earth's climate and its predictability over the last 66 million years. *Science*, 369(6509), 1383–1387. <https://doi.org/10.1126/science.aba6853>
- Wu, B., & Wang, J. (2002). Winter Arctic oscillation, Siberian high and East Asian winter monsoon. *Geophysical Research Letters*, 29(19), 3–13. <https://doi.org/10.1029/2002GL015373>
- Wyrwoll, K.-H., Wei, J., Lin, Z., Shao, Y., & He, F. (2016). Cold surges and dust events: Establishing the link between the East Asian Winter Monsoon and the Chinese loess record. *Quaternary Science Reviews*, 149, 102–108. <https://doi.org/10.1016/j.quascirev.2016.04.015>
- Xie, J., Wu, F., & Ding, Z. (2007). Detrital zircon composition of U-Pb ages and Hf isotope of the Hunshadake sandland and implications for its provenance. *Acta Petrologica Sinica*, 23(2), 523–528.
- Yang, J., Gao, S., Chen, C., Tang, Y., Yuan, H., Gong, H., et al. (2009). Episodic crustal growth of North China as revealed by U-Pb age and Hf isotopes of detrital zircons from modern rivers. *Geochimica et Cosmochimica Acta*, 73(9), 2660–2673. <https://doi.org/10.1016/j.gca.2009.02.007>
- Zhang, H., Lu, H., He, J., Xie, W., Wang, H., Zhang, H., et al. (2022). Large-number detrital zircon U-Pb ages reveal global cooling caused the formation of the Chinese Loess Plateau during Late Miocene. *Science Advances*, 8(41), eabq2007. <https://doi.org/10.1126/sciadv.abq2007>
- Zhang, H., Lu, H., Xu, X., Liu, X., Yang, T., Stevens, T., et al. (2016). Quantitative estimation of the contribution of dust sources to Chinese loess using detrital zircon U-Pb age patterns. *JGR Earth Surface*, 121(11), 2085–2099. <https://doi.org/10.1002/2016jf003936>
- Zhang, R., Jiang, D., Ramstein, G., Zhang, Z., Lippert, P. C., & Yu, E. (2018). Changes in Tibetan plateau latitude as an important factor for understanding East Asian climate since the Eocene: A modeling study. *Earth and Planetary Science Letters*, 484, 295–308. <https://doi.org/10.1016/j.epsl.2017.12.034>
- Zhang, R., Kravchinsky, V. A., Zhu, R., & Yue, L. (2010). Paleomonsoon route reconstruction along a W–E transect in the Chinese Loess Plateau using the anisotropy of magnetic susceptibility: Summer monsoon model. *Earth and Planetary Science Letters*, 299(3), 436–446. <https://doi.org/10.1016/j.epsl.2010.09.026>
- Zhang, Y., Sperber, K. R., & Boyle, J. S. (1997). Climatology and interannual variation of the East Asian winter monsoon: Results from the 1979–95 NCEP/NCAR reanalysis. *Monthly Weather Review*, 125(10), 2605–2619. [https://doi.org/10.1175/1520-0493\(1997\)125<2605:CAIVOT>2.0.CO;2](https://doi.org/10.1175/1520-0493(1997)125<2605:CAIVOT>2.0.CO;2)
- Zhang, Z., Liu, Y., Wang, L., Kaakinen, A., Wang, J., Mao, F., & Tong, Y. (2016). Lithostratigraphic context of Oligocene mammalian faunas from Ulanatal, Nei Mongol, China. *Comptes Rendus Palevol*, 15(7), 903–910. <https://doi.org/10.1016/j.crpv.2015.05.012>
- Zhao, H., Liu, C., Wang, F., Wang, J., Li, Q., & Yao, Y. (2007). Uplift and evolution of Helan mountain. *Science in China Series D: Earth Sciences*, 50(2), 217–226. <https://doi.org/10.1007/s11430-007-6010-5>
- Zhu, R., Liu, Q., & Jackson, M. J. (2004). Paleoenvironmental significance of the magnetic fabrics in Chinese loess-paleosols since the last interglacial (<130 ka). *Earth and Planetary Science Letters*, 221(1), 55–69. [https://doi.org/10.1016/S0012-821X\(04\)00103-7](https://doi.org/10.1016/S0012-821X(04)00103-7)